AUTOMATION
IN
ROUGH TURNING

BY

PO LUNG WOO

A Thesis
Submitted to the Faculty of Graduate Studies
in Partial Fulfillment of the Requirements
for the Degree of

MASTER OF SCIENCE

Department of Mechanical and Industrial Engineering
University of Manitoba
Winnipeg, Manitoba

ISBN 0-612-13573-X

Name _____

Dissertation Abstracts International and *Masters Abstracts International* are arranged by broad, general subject categories. Please select the one subject which most nearly describes the content of your dissertation or thesis. Enter the corresponding four-digit code in the spaces provided.

ENGINEERING MECHANICAL

SUBJECT TERM

0548

SUBJECT CODE

UMI

Subject Categories

THE HUMANITIES AND SOCIAL SCIENCES

COMMUNICATIONS AND THE ARTS
Architecture 0729
Art History 0377
Cinema 0900
Dance 0378
Fine Arts 0357
Information Science 0723
Journalism 0391
Library Science 0399
Mass Communications 0708
Music 0413
Speech Communication 0459
Theater 0465

EDUCATION
General 0515
Administration 0514
Adult and Continuing 0516
Agricultural 0517
Art 0273
Bilingual and Multicultural 0282
Business 0688
Community College 0275
Curriculum and Instruction 0727
Early Childhood 0518
Elementary 0524
Finance 0277
Guidance and Counseling 0519
Health 0680
Higher 0745
History of 0520
Home Economics 0278
Industrial 0521
Language and Literature 0279
Mathematics 0280
Music 0522
Philosophy of 0998
Physical 0523
Psychology 0525
Reading 0535
Religious 0527
Sciences 0714
Secondary 0533
Social Sciences 0534
Sociology of 0340
Special 0529
Teacher Training 0530
Technology 0710
Tests and Measurements 0288
Vocational 0747

LANGUAGE, LITERATURE AND LINGUISTICS
Language
- General 0679
- Ancient 0289
- Linguistics 0290
- Modern 0291

Literature
- General 0401
- Classical 0294
- Comparative 0295
- Medieval 0297
- Modern 0298
- African 0316
- American 0591
- Asian 0305
- Canadian (English) 0352
- Canadian (French) 0355
- English 0593
- Germanic 0311
- Latin American 0312
- Middle Eastern 0315
- Romance 0313
- Slavic and East European 0314

PHILOSOPHY, RELIGION AND THEOLOGY
Philosophy 0422
Religion
- General 0318
- Biblical Studies 0321
- Clergy 0319
- History of 0320
- Philosophy of 0322

Theology 0469

SOCIAL SCIENCES
American Studies 0323
Anthropology
- Archaeology 0324
- Cultural 0326
- Physical 0327

Business Administration
- General 0310
- Accounting 0272
- Banking 0770
- Management 0454
- Marketing 0338

Canadian Studies 0385
Economics
- General 0501
- Agricultural 0503
- Commerce-Business 0505
- Finance 0508
- History 0509
- Labor 0510
- Theory 0511

Folklore 0358
Geography 0366
Gerontology 0351
History
- General 0578
- Ancient 0579
- Medieval 0581
- Modern 0582
- Black 0328
- African 0331
- Asia, Australia and Oceania 0332
- Canadian 0334
- European 0335
- Latin American 0336
- Middle Eastern 0333
- United States 0337

History of Science 0585
Law 0398
Political Science
- General 0615
- International Law and Relations 0616
- Public Administration 0617

Recreation 0814
Social Work 0452
Sociology
- General 0626
- Criminology and Penology ... 0627
- Demography 0938
- Ethnic and Racial Studies 0631
- Individual and Family Studies 0628
- Industrial and Labor Relations 0629
- Public and Social Welfare 0630
- Social Structure and Development 0700
- Theory and Methods 0344

Transportation 0709
Urban and Regional Planning 0999
Women's Studies 0453

THE SCIENCES AND ENGINEERING

BIOLOGICAL SCIENCES
Agriculture
- General 0473
- Agronomy 0285
- Animal Culture and Nutrition 0475
- Animal Pathology 0476
- Food Science and Technology 0359
- Forestry and Wildlife 0478
- Plant Culture 0479
- Plant Pathology 0480
- Plant Physiology 0817
- Range Management 0777
- Wood Technology 0746

Biology
- General 0306
- Anatomy 0287
- Biostatistics 0308
- Botany 0309
- Cell 0379
- Ecology 0329
- Entomology 0353
- Genetics 0369
- Limnology 0793
- Microbiology 0410
- Molecular 0307
- Neuroscience 0317
- Oceanography 0416
- Physiology 0433
- Radiation 0821
- Veterinary Science 0778
- Zoology 0472

Biophysics
- General 0786
- Medical 0760

EARTH SCIENCES
Biogeochemistry 0425
Geochemistry 0996
Geodesy 0370
Geology 0372
Geophysics 0373
Hydrology 0388
Mineralogy 0411
Paleobotany 0345
Paleoecology 0426
Paleontology 0418
Paleozoology 0985
Palynology 0427
Physical Geography 0368
Physical Oceanography 0415

HEALTH AND ENVIRONMENTAL SCIENCES
Environmental Sciences 0768
Health Sciences
- General 0566
- Audiology 0300
- Chemotherapy 0992
- Dentistry 0567
- Education 0350
- Hospital Management 0769
- Human Development 0758
- Immunology 0982
- Medicine and Surgery 0564
- Mental Health 0347
- Nursing 0569
- Nutrition 0570
- Obstetrics and Gynecology .. 0380
- Occupational Health and Therapy 0354
- Ophthalmology 0381
- Pathology 0571
- Pharmacology 0419
- Pharmacy 0572
- Physical Therapy 0382
- Public Health 0573
- Radiology 0574
- Recreation 0575
- Speech Pathology 0460
- Toxicology 0383

Home Economics 0386

PHYSICAL SCIENCES
Pure Sciences
Chemistry
- General 0485
- Agricultural 0749
- Analytical 0486
- Biochemistry 0487
- Inorganic 0488
- Nuclear 0738
- Organic 0490
- Pharmaceutical 0491
- Physical 0494
- Polymer 0495
- Radiation 0754

Mathematics 0405
Physics
- General 0605
- Acoustics 0986
- Astronomy and Astrophysics 0606
- Atmospheric Science 0608
- Atomic 0748
- Electronics and Electricity 0607
- Elementary Particles and High Energy 0798
- Fluid and Plasma 0759
- Molecular 0609
- Nuclear 0610
- Optics 0752
- Radiation 0756
- Solid State 0611

Statistics 0463

Applied Sciences
Applied Mechanics 0346
Computer Science 0984
Engineering
- General 0537
- Aerospace 0538
- Agricultural 0539
- Automotive 0540
- Biomedical 0541
- Chemical 0542
- Civil 0543
- Electronics and Electrical 0544
- Heat and Thermodynamics ... 0348
- Hydraulic 0545
- Industrial 0546
- Marine 0547
- Materials Science 0794
- Mechanical 0548
- Metallurgy 0743
- Mining 0551
- Nuclear 0552
- Packaging 0549
- Petroleum 0765
- Sanitary and Municipal 0554
- System Science 0790

Geotechnology 0428
Operations Research 0796
Plastics Technology 0795
Textile Technology 0994

PSYCHOLOGY
General 0621
Behavioral 0384
Clinical 0622
Developmental 0620
Experimental 0623
Industrial 0624
Personality 0625
Physiological 0989
Psychobiology 0349
Psychometrics 0632
Social 0451

AUTOMATION IN ROUGH TURNING

BY

PO LUNG WOO

A Thesis submitted to the Faculty of Graduate Studies of the University of Manitoba in partial fulfillment of the requirements of the degree of

MASTER OF SCIENCE

ACKNOWLEDGMENTS

I wish to take this opportunity to thank Professor N. Popplewell and Professor S. Balakrishnan for their invaluable and patient guidance through the entire research. Under their supervision, my knowledge in the engineering field especially in automation is undoubtedly improved. I should also acknowledge with gratitude the help that I have received from Professor N. Popplewell during the preparation of this thesis. I am honoured to have them as my supervisors. Hence, I will do my best in my future engineer's career to show my appreciation for their training. I also wish my success can be as great as their success.

I appreciate the help from Professor D. Rajamani for helping me in the area of integer programming. Special thanks also goes to the skilful and friendly technicians, F. Kapitoler, K. Tarte, B. Barrett, and I. Penner, in the Department of Mechanical and Industrial Engineering. They not only helped me to solve technical problems, but also taught me how to broaden my knowledge in the practical aspects.

I also owe my family the greatest thankfulness for their support. I especially wish to thank my wife, Leanne, whose encouragement is the biggest motivation which led me to a successful education.

ABSTRACT

An inexpensive laser-based device is attached to a microcomputer controlled lathe to form an intelligent material turning system. The device is based upon the photocell detection of a laser beam that laterally strikes the workpiece so as to be blocked intermittently. It is designed to monitor machining chatter and extraneous vibrations, to detect tool breakage, to map a workpiece's spinning profile, and to perform a preliminary quality inspection. The integration of these functions, in addition to a new cutting strategy and computerized selection of cutting parameters, leads automatically to the maximum material removal rate during rough turning. A prototype is found to be capable of sensing a change of ±0.025 mm in the diameter of a cylinder, for example, regardless of the cylinder's color, size and surface condition, the ambient lighting, or whether a cutting fluid is employed. This accuracy is more than adequate for rough turning. Experiments show that the reduction in time, compared with conventional cutting, depends strongly upon a workpiece's profile but the saving can be as high as 36%.

LIST OF FIGURES

		Page
Figure 2.1.	Formation of Spinning Profiles.	4
Figure 2.2.	Side View of a Rotating Square Block and Its Image.	4
Figure 2.3.	The Prototype Device.	5
Figure 2.4.	Angular Relationship Between Mirror and Sensor for Synchronization.	7
Figure 2.5.	Sensor's Structure and the Divider Circuit.	7
Figure 2.6.	Showing (a) the Setup to Find the Sensor's Sensitivity, and (b) Side View of the Laser Beam.	9
Figure 2.7.	Sensitivity of Sensor.	9
Figure 2.8.	Conversion Curve for the Output Voltage.	10
Figure 2.9.	Relative Displacement Between the Sensor's Pin Hole and the Laser Spot.	11
Figure 2.10.	Setup to Measure the Sensor's Time Response.	12
Figure 2.11.	Signal Caused by Protrusion.	13
Figure 2.12.	Interrupted Signal shown by Sudden Change in Magnitude of Relative Velocity.	13
Figure 3.1.	Elements of Cutting in Turning.	14
Figure 3.2.	The Major Components of a Lathe.	15
Figure 3.3.	Upper Portion of a Symmetrical Profile.	20
Figure 3.4.	Tool Path for Conventional Cutting.	21
Figure 3.5.	Profile Grid and Numbered Tool Locations.	22
Figure 3.6.	Tool Path Determined Heuristically.	22
Figure 3.7.	First LINDO Solution.	25

Figure 3.8.	Second Solution Adding $X_{6,4}=0$ into the Constraints.	26
Figure 3.9.	Third Solution Adding $X_{1,4}=0$ into the Constraints.	27
Figure 3.10.	Fourth Solution Adding $X_{1,3}=0$ into the Constraints.	27
Figure 3.11.	Fifth Solution Adding $X_{5,4}=0$ into the Constraints.	28
Figure 3.12.	Optimal Solution.	28
Figure 4.1.	Experimental Setup.	31
Figure 4.2.	Illustrating Synchronization. (a) Locations of Arm, (b) Relative Displacement, and (c) Noise Represented by Relative Velocity.	34
Figure 4.3.	Scan of a Cylinder Showing (a) Locations of Arm, (b) Relative Displacement, and (c) Relative Velocity.	36
Figure 4.4.	Scan of a Cylinder Having a Protrusion and Rotating at 1100 RPM. Showing (a) Locations of Arm, (b) Relative Displacement, and (c) Relative Velocity.	37
Figure 4.5.	Relationship Between Duration of Laser Beam's Blockage to a Shaft's Diameter.	39
Figure 4.6.	Different Initial Contact Positions of Laser Beam and Protrusion.	40
Figure 4.7.	Speed Factors Affecting R_{error}.	42
Figure 4.8.	A Comparison of t_o(s) Obtained at 200 RPM.	44
Figure 4.9.	A Comparison of t_o(s) Obtained for the Same Cylinder Rotating at 2289 RPM.	45
Figure 4.10.	(a) Change of Measured Profile at Different Increment in Z-axis, and (b) Example of Calculation of the RMS Difference Between the Reference and Measured Profiles at $S_{z\text{-}axis}=1.0$ mm.	48
Figure 4.11.	Showing (a) Comparison of Measured and Reference Step Profiles, and (b) % Error in Diameter along the Workpiece's Length.	50
Figure 4.12.	Showing (a) Comparison of Measured and Reference Profiles, and (b) % Error in Diameter along the Workpiece's Length.	51

Figure 4.13.	Showing (a) Inner and Outer Profiles of a Spinning, Asymmetrical Workpiece, and (b) % Error in Diameter along the Workpiece's Length.	52
Figure 4.14.	Comparison of Tool Paths Between (a) Conventional and (b) Optimal Solution for the Profile of Figure 4.11(a).	54
Figure 4.15.	Optimal Tool Path for Profile of Figure 4.12(a).	55
Figure 4.16.	Showing the Displacement at a Spindle Speed of (a) 658 RPM (11.0 Hz), and (b) 1159 RPM (19.3 Hz).	57
Figure 4.17.	Cutting Signal when Depths of Cut were a Constant (a) 3.0 mm, (b) 4.0 mm, (c) 4.5 mm, and (d) 5.0 mm.	59
Figure 4.18	Relationship Between Depth of Cut and Rd_{max}.	60
Figure 4.19.	Output when Depth of Cut was Modified.	61
Figure 4.20.	Signal Indicating Tool Breakage.	63
Figure 5.1.	Shapes and Uses of Common, Single-point Lathe Tools.	65
Figure A.1.	Side View of a Laser Beam Blocked by an Object.	70
Figure A.2.	Relative Displacement Between the Sensor's Pinhole and Laser Spot.	71

LIST OF TABLES

		Page
Table 3.1.	Traditional Cutting Parameters for Low Carbon Steel and a High Speed Steel Tool [8].	17
Table 3.2.	Interpolated Feed and Cutting Speed for 1.5 mm Cutting Depth.	18
Table 3.3.	Time Matrix for Tool Locations.	24
Table 4.1.	Shaft's Diameter Measured at 200 RPM and 2289 RPM.	43
Table 4.2.	Time (in s) Spent on Travelling Each Segment shown in (a) Figure 4.14(b), (b) Figure 4.15, and (c) the Time Saved by New Cutting Strategy.	56

TABLE OF CONTENTS

	Page
ACKNOWLEDGMENT	ii
ABSTRACT	iii
LIST OF FIGURES	iv
LIST OF TABLES	vii
TABLE OF CONTENTS	viii
CHAPTER 1 INTRODUCTION	1
CHAPTER 2 THE MEASUREMENT DEVICE	3
2.1 Formation of Spinning Profiles	3
2.2 The Prototype Device	5
2.3 Sensor	7
2.3.1 Relationship Between Light Intensity and Output Voltage	8
2.3.2 Interpretation of the Sensor's Output Voltage	10
2.3.3 Sensor's Time Response	12
CHAPTER 3 ROUGH TURNING	14
3.1 Selection of Cutting Parameters in Rough Turning	16
3.1.1 Required Motor Power for Cutting	17
3.1.2 Estimation of Maximum Permissible Depth of Cut	18
3.2 Determination of Tool Cutting Sequence	19
3.2.1 Conventional Cutting	20
3.2.2 New Heuristic Approach to Cutting	21
3.2.3 Validation of New Strategy	23
3.2.4 Example of Time Saving from the New Cutting Strategy	29
CHAPTER 4 EXPERIMENTS AND RESULTS	30
4.1 Hardware	30
4.1.1 Interfacing	31
4.2 Profile Mapping	32
4.2.1 Synchronization of Laser Beam and Sensor	33
4.2.2 Selection of Threshold's Upper Limit	35
4.2.3 Conversion of Measured Signal into an Equivalent Shaft Diameter	38
4.3 Factors Affecting the Performance of the Prototype	39
4.3.1 Speed Factors in Measurement Accuracy	40
4.3.1.1 Results at Different Rotational Speeds	42

4.3.1.2 Command of the Scanning Speed 46
4.3.2 Effect of Laser's Spot Size and Travel Increment 46
4.4 Results of Profile Mapping 48
4.5 Results of Automation and New Cutting Strategy 53
4.6 Results of Vibration Detection 56
4.7 Results of Chatter Suppression 58
4.7.1 Relating Extraneous Vibration to Different Depth of Cuts 58
4.7.2 Closed-loop Control To Suppress Extraneous Vibration 60
4.8 Detection of Tool Breakage 61
CHAPTER 5 CONCLUSIONS AND RECOMMENDATIONS 64
REFERENCES 67
APPENDIX A 70

CHAPTER 1
INTRODUCTION

Metal cutting such as grinding, shaping, drilling, milling ,or turning is the most important and widely used manufacturing process. Although the practical details of these processes differ, they all involve removing unwanted material from a workpiece by using a cutting tool. Such a procedure is exemplified presently by the turning of an initially arbitrarily shaped workpiece on a readily available but small (1.9 hp), precision lathe. Turning generally involves rough cutting to quickly shape a workpiece without violating dimensional constraints followed by finish cutting to meet precise size and surface finish specifications. A partially automated finishing process employing laser measurements has been described previously [1-5] so that only a complementary and completely automated approach to rough cutting is presented here.

A major concern in rough turning is to maximize the material removal rate (MRR), without sacrificing the tool life, by optimizing the two variables, namely feedrate or depth of cut. In a conventional turning these variables are selected manually at the beginning of the process by using empirical data based upon the size and material properties of the workpiece as well as the type of cutting tool employed. They remain unchanged throughout and, primarily for safety, they tend to be conservative. One strategy to reduce cutting time by about a half [6] involves maintaining the maximum cutting force by adaptively changing the feedrate. A higher feedrate, however, substantially reduces the cutting tool's life which could lengthen the manufacturing cycle because of more frequent tool replacements. This technique is also adopted in conjunction with "softening" the workpiece by employing a CO_2 laser [7]. In this case, a 100% increase is achieved in the MMR without decreasing the tool life. On the other hand, a CO_2 laser is expensive and its application in industrial rough cutting is impractical because of the difficulty of using optical systems in an adverse environment of "flying" metal chips and cutting fluid.

A larger depth of cut will obviously increase the MRR but experimental results suggest that chatter (i.e. detrimental vibrations of the workpiece) is more likely to occur [8]. Even so, the depth of cut is usually selected to be close to the upper limit determined from the lathe's maximum power. In the following work, the depth of cut is kept constant but close to the upper limit, and monitored throughout the cutting process. This approach leads to a concern that detrimental vibrations should be avoided. Therefore, a preliminary experiment is conducted to confirm that a real time reduction in the depth of cut could be used to effectively suppress the vibration initiated at a larger cutting depth.

Rough cutting is begun with an unknown or arbitrarily shaped workpiece, that could be a scrap piece. Therefore, it is essential to determine the workpiece's dimensions in order to select the cutting parameters. A laser is commonly incorporated in devices for mapping a profile [9-19]. Measurement techniques involve finding the time of flight of a reflected laser beam, analyzing changing patterns of the reflection of structured light, correlating the surface curvature and laser scattered patterns, or determining a change in the intensity of a reflected laser beam caused by different distances from an object. Nevertheless, these techniques are limited by the variability in a workpiece's appearance (for example a restriction in size and shape), an insensitivity to dark colors, and a difference in an object's roughness. A laser-based measurement device has been designed to avoid these shortcomings. It can be used to obtain the spinning profile of any arbitrarily shaped workpiece, under normal machine shop conditions. Details of the device are described in Chapter 2. If a scanning result shows that a workpiece has a highly variable cross-section, modification of the feedrate and tool relocation can also benefit the MRR. This modified cutting strategy is demonstrated to be as much as 36% faster than a conventional approach. It is described in Chapter 3.

Finally, details of the experimental setup as well as test results are presented in Chapter 4. The last chapter gives conclusions, proposed applications and recommends further improvements.

CHAPTER 2
THE MEASUREMENT DEVICE

The geometry of a part can be found by using a variety of contact techniques that range from manual measurements, with calipers or micrometer, to an automated determination employing a touch probe mounted on a coordinate measurement machine. Such measurements, however, must be performed on a stationary object or the object must be transported to a stand-alone device. Unfortunately, once a part is unloaded from a machine for inspection, difficulty in precisely reloading the workpiece for further processing might extend the manufacturing cycle or even result in a scrap product. A non-contact measurement device could overcome such a problem.

2.1 Formation of Spinning Profiles

A workpiece for turning could be a cylinder, a rectangular bar or even arbitrarily shaped, but all such objects are effectively piecewise conical when spun. For example, the profiles produced by an illuminated square bar that spins are illustrated in Figure 2.1. A uniform light shines from above the rigid bar which rotates about its geometric center. Two different grey levels images can be seen to be formed on a plane screen placed underneath the bar. The grey region is due to the intermittent interruption of light caused by the rotation of the bar's four corners. The dark region, conversely, corresponds to a complete absence of light due to total blockage by the bar's core. The borders between the dark and grey regions are called inside profiles whereas those between the grey and bright regions are outside profiles. Half the distance between the two outside profiles indicates the cutting tool's minimum starting offset, C_{offset}, and half that between the inside profiles gives the maximum radius, R, that can be manufactured for a cylinder.

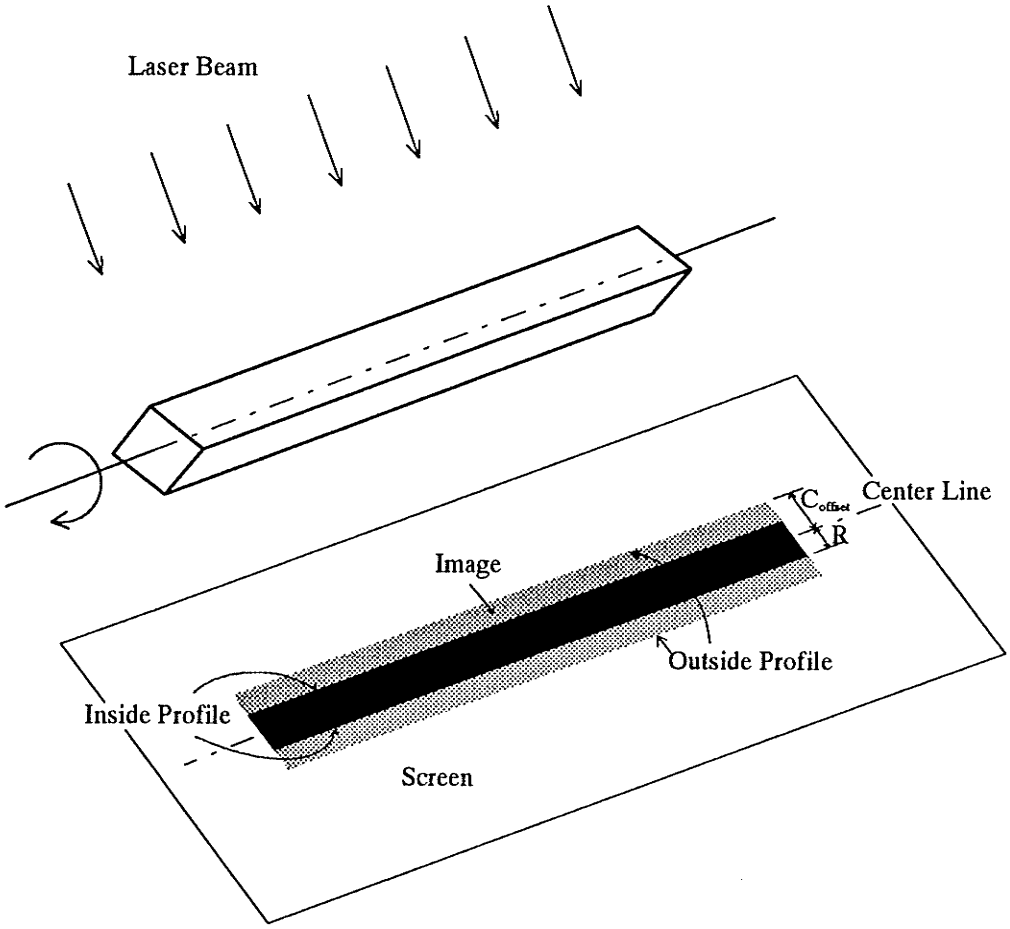

Figure 2.1. Formation of Spinning Profiles.

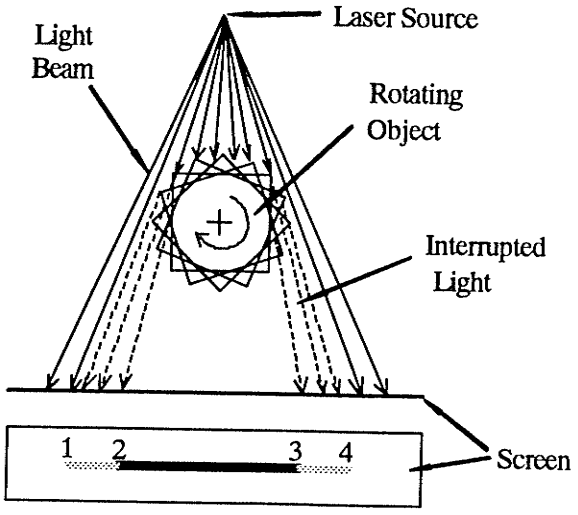

Figure 2.2. Side View of a Rotating Square Block and Its Image.

Profiles are described in Figure 2.2 by interpolating a series of points that are extracted from the line image formed underneath the rotating square bar. There are four locations numbered 1 through 4 where the grey level changes. Due to symmetry, either points 1 and 2, or points 3 and 4 are sufficient for reconstructing the profiles. This technique of reconstructing profiles is equally applicable to any other irregular workpiece, as illustrated in Chapter 4.

2.2 The Prototype Device

The major components of the device used to map the inside and outside profiles of any workpiece include a laser source, a sensor, gear train, rigid arm, two mirrors and a stepper motor. This device is represented schematically in Figure 2.3.

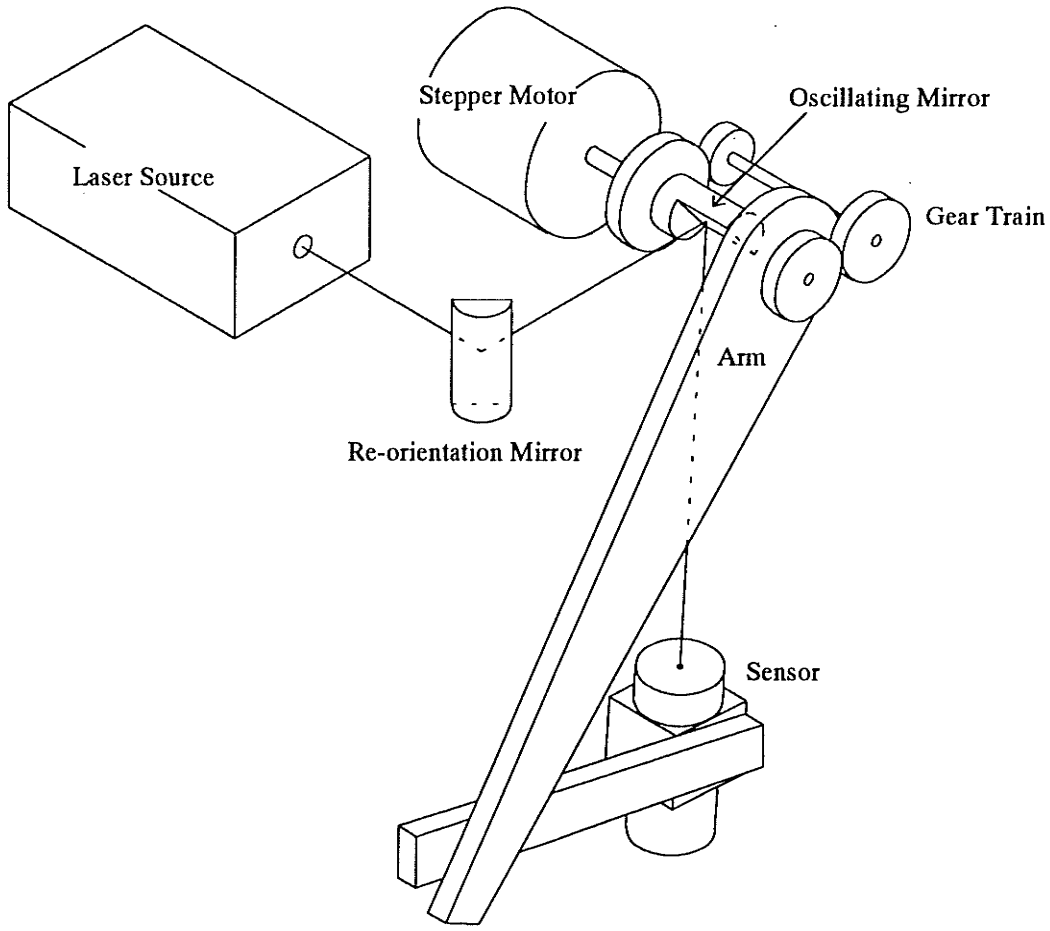

Figure 2.3. The Prototype Device.

The light source is a Uniphase, 155SL He-Ne laser because a parallel light beam is required. The light beam is redirected first by the re-orientation mirror, and then it hits the oscillating mirror. Hence, the light beam is swept across a cross-section of the spinning workpiece by using the reflection from an oscillating mirror when the stepper motor is pulsed to move. The locus of the reflected light is captured by a sensor which is held near the end of a rigid arm. The sensor's motion is controlled in order to follow the path of the reflected light beam. Synchronization is achieved by using a gear train which connects the oscillating mirror and the arm.

In order to synchronize the motion of the oscillating mirror and sensor, two conditions must be satisfied. The first condition is that they must share the same center of rotation. The second condition is that the sensor must rotate twice the change in the angle of the oscillating mirror. It can be seen from Figure 2.4 that the oscillating mirror and the sensor are configured to share the same center of rotation. Moreover, the light beam is hit at the center of rotation of the oscillating mirror and then reflects to hit the sensor. With this arrangement, if the oscillating mirror rotates through an angle θ, the sensor must rotate 2θ in the same direction to capture the reflected light beam. It is assumed that the angles formed between the incident and reflected light beams for the sensor's initial and second position are β and β', respectively. Now β is the sum of incident, i, and reflected, r, angles. When the oscillating mirror rotates through an angle θ, the normal of the mirror also rotates through θ. Hence,

$$i' = i - \theta, \text{ and } r' = r - \theta$$

because

$$\beta' = i' + r' = (i - \theta) + (r - \theta) = i + r - 2\theta = \beta - 2\theta.$$

Therefore, the sensor must rotate 2θ to capture the reflected light beam whenever the oscillating mirror is rotated by θ. Consequently, a gear train having a 2:1 gear ratio should interconnect the mirror and sensor.

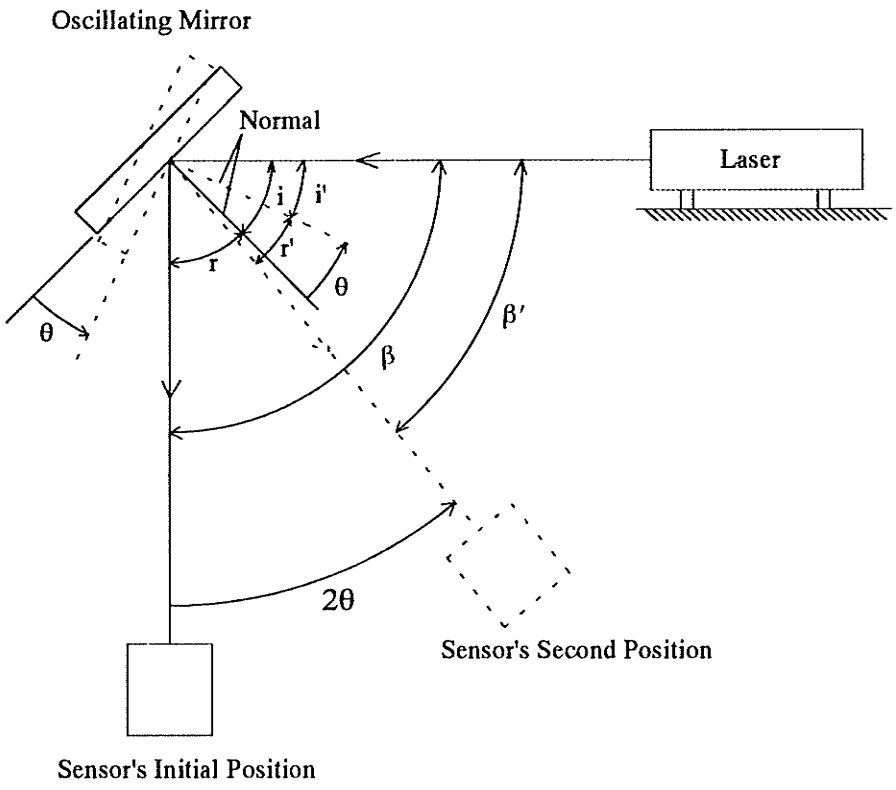

Figure 2.4. Angular Relationship Between Mirror and Sensor for Synchronization.

2.3 Sensor

The sensor, which is represented in Figure 2.5, contains a 1 mm diameter pin hole, two concave lens, and a photocell (part No. V276353 90-153-0 from Electro Sonic Inc.).

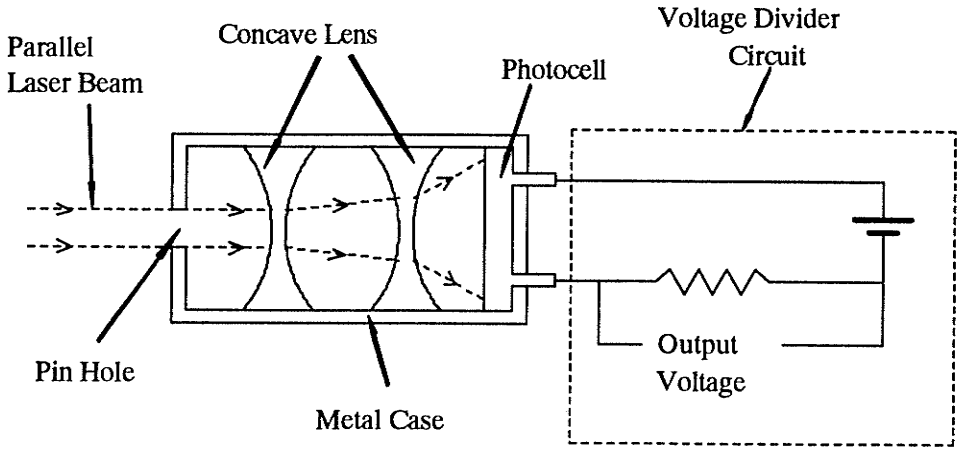

Figure 2.5. Sensor's Structure and the Divider Circuit.

The pin hole is sufficiently small that ambient room lighting is effectively excluded. The laser light diverges at the two concave lens into a 10 mm diameter circle in order to completely cover the photocell's surface for greater sensitivity. The photocell behaves as a light-controlled, variable resistor whose resistance is increased from about 500 Ω, when exposed to the laser light, to approximately 4 MΩ when isolated from this light. Therefore, when the sensor is used in conjunction with a voltage divider circuit, a voltage output can be obtained that corresponds to the intensity of the incident light.

2.3.1 Relationship Between Light Intensity and Output Voltage

The experimental setup to determine the relationship between the sensor's voltage and the light intensity is illustrated in Figure 2.6(a). Both the laser source and the sensor are aligned and fixed in the following procedures. The laser source is first located and fixed on a solid horizontal surface, then the sensor is located about 300 mm from the laser source on the same surface. The position of the sensor is fine tuned until a reading of 3.6 V is indicated on the multimeter. Then, the sensor is exposed to the full light intensity. A cylinder is moved transversely across the laser beam to effectively reduce the laser beam's width and, hence, the amount of light entering the sensor's pin hole. The initial position of the cylinder is the location where the laser beam begins to be blocked by the cylinder. This location is determined when a tiny red light spot is observed on the cylinder's surface. The cylinder's displacement, D, is measured by using a dial gage to an accuracy within ± 0.013 mm. The output voltage of the sensor is found from a Keithley 169 multimeter. The voltage readings for 0.025 mm increments in the displacement, D, are plotted in Figure 2.7. The plot shows a dramatic change in the photocell's resistance once the laser beam's width is blocked by more than about half. Thus the photocell is saturated until the light intensity decreases to about half after which, the substantial change in the voltage value, corresponding to each 0.025 mm increment, indicates that the sensor has good sensitivity to light intensity changes in this "employed" region.

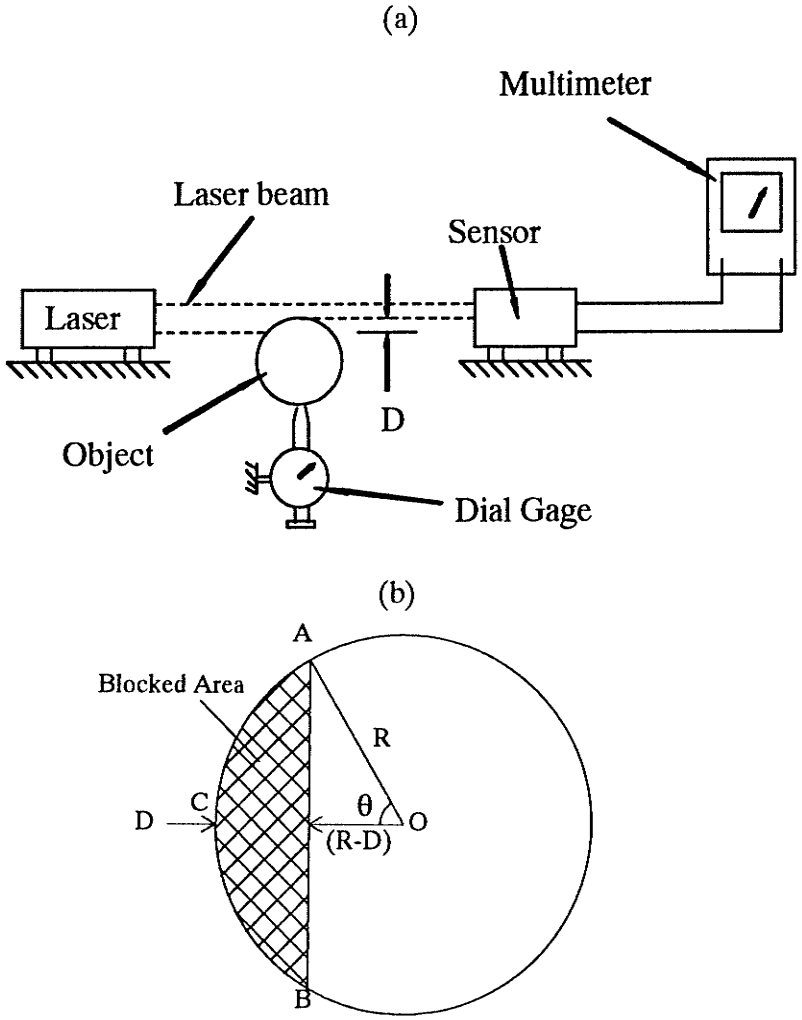

Figure 2.6. Showing (a) the Setup to Find the Sensor's Sensitivity, and (b) Side View of the Laser Beam.

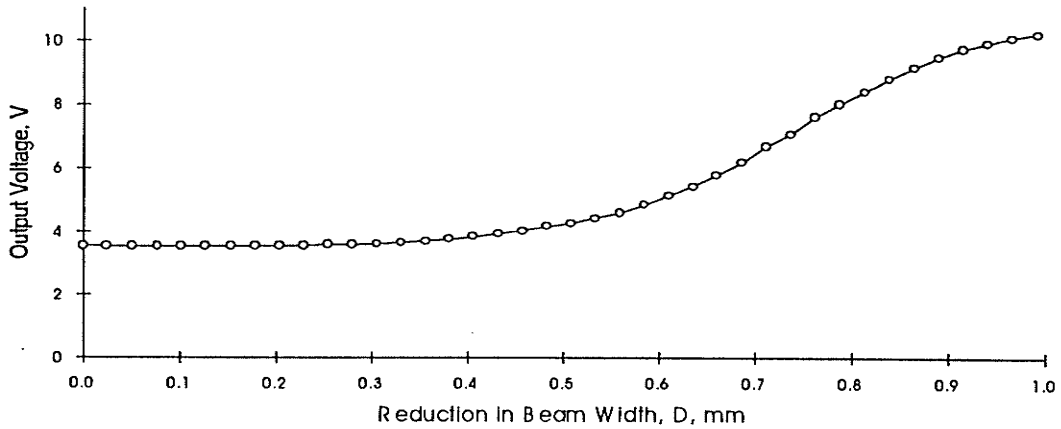

Figure 2.7. Sensitivity of Sensor.

2.3.2 Interpretation of the Sensor's Output Voltage

The sensor's output voltage can be interpreted as the amount of the laser beam's spot blocked by an object. Figure 2.6(b) shows the laser beam's spot, which has a radius R, when it is blocked partially by a cylinder. The relationship between the percent reduction in the area of the spot, dA, to the corresponding reduction in the beam's width, D, is described by the following equation:

$$dA = \begin{cases} \dfrac{\dfrac{\theta\pi R^2}{180} - (R - D)R\sin\theta}{\pi R^2} \times 100\%, & D \le R \\ \dfrac{\dfrac{\theta\pi R^2}{180} + (R - D)R\sin\theta}{\pi R^2} \times 100\%, & D > R, \end{cases} \qquad (2.1)$$

where R= radius, in mm, of the laser spot,

$\theta = \cos^{-1}(1-D/R)$, in degrees.

The derivation of the above equation is given more conveniently in Appendix A. By employing this equation, Figure 2.7 is replotted in Figure 2.8 to give the percent reduction in the spot's area as a function of the output voltage.

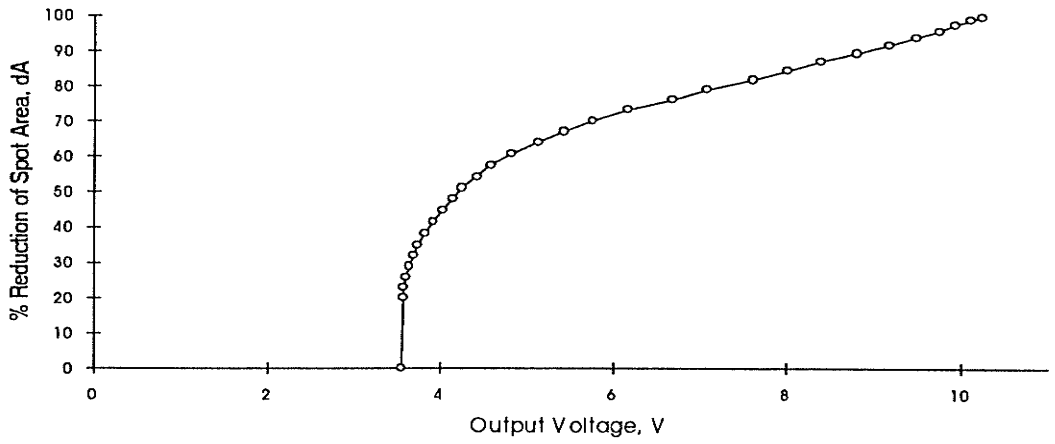

Figure 2.8. Conversion Curve for the Output Voltage.

The sensor's output voltage can also be interpreted in terms of the relative displacement, R_d, between the sensor's pin hole and the laser spot, as shown in Figure 2.9.

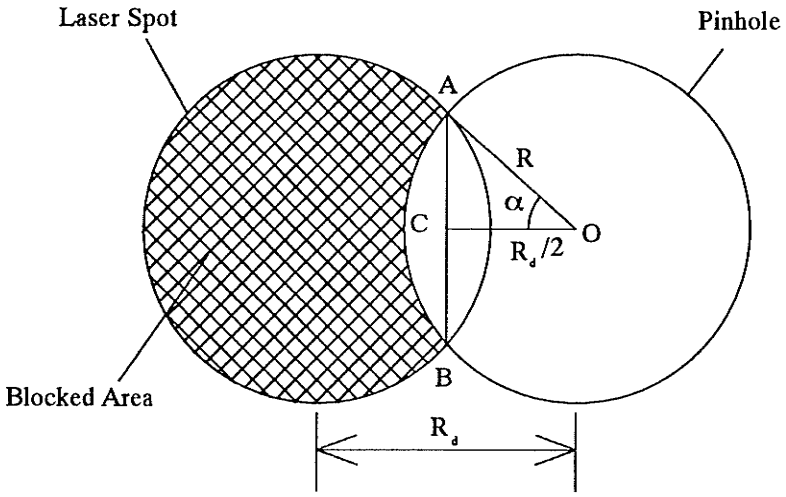

Figure 2.9. Relative Displacement Between the Sensor's Pinhole and the Laser Spot.

If the laser spot coincides with the sensor's pin hole, the sensor will receive the full light intensity and give an output voltage of 3.6 V. However, if a relative displacement occurs between the sensor's pinhole and the laser spot due to vibration or misalignment, the output voltage changes and a higher value of dA is obtained. The new value of dA is then used to compute the R_d by using the following equations which are derived again in Appendix A.

$$R_d = 2R\cos\alpha \tag{2.2}$$

where α , in degrees, is given by:

$$\pi\left(1-\frac{dA}{100}\right) = \left(\frac{\pi\alpha}{90} - \sin 2\alpha\right). \tag{2.3}$$

A technique called Bisection Method [20] is used to find angle α from equation (2.3).

2.3.3 Sensor's Time Response

The sensor's time response is determined by using the experimental setup illustrated in Figure 2.10.

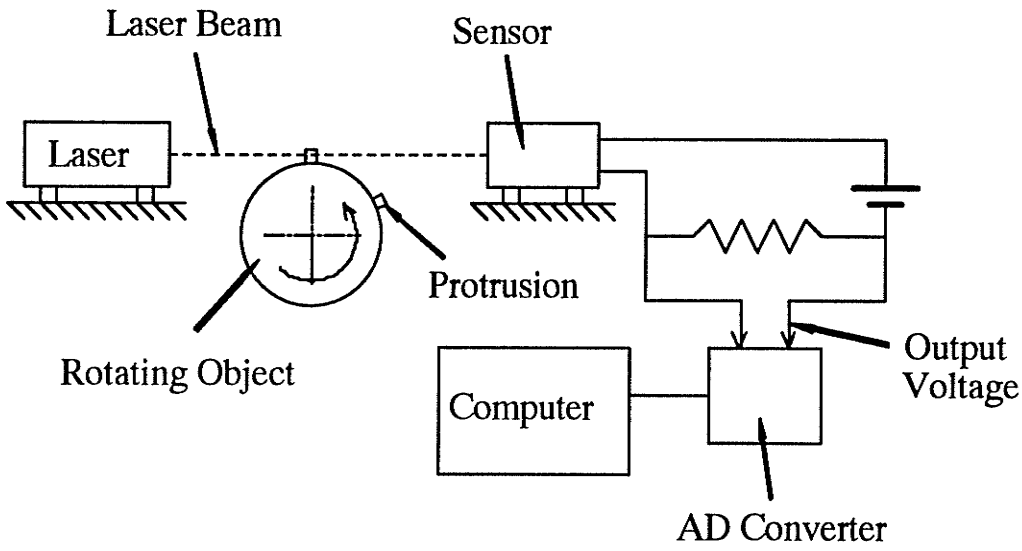

Figure 2.10 Setup to Measure the Sensor's Time Response.

The laser source and sensor remain stationary and a cylinder, having a diameter of 34.7 mm and a thin metal protrusion with a height of 8.5 mm, is rotated at a constant speed of 330 RPM (5.5 Hz). The laser beam is interrupted by the protrusion once every cycle of the cylinder's rotation and the sensor's output is changed correspondingly. A voltage divider circuit is employed to convert the photocell's resistance to an analogous voltage. The voltage is converted to dA by using the curve in Figure 2.8. Then dA is used to calculate the relative displacement, R_d, by using equations (2.2) and (2.3). Data is acquired automatically at 1980 Hz by using an analog to digital (AD) converter. Consequently, 360 samples are taken for each revolution and they are displayed in Figure

2.11. The plot shows that the sensor requires only 0.04 s to respond to a change in the light intensity from bright to dark when the relative displacement equals 1 mm.

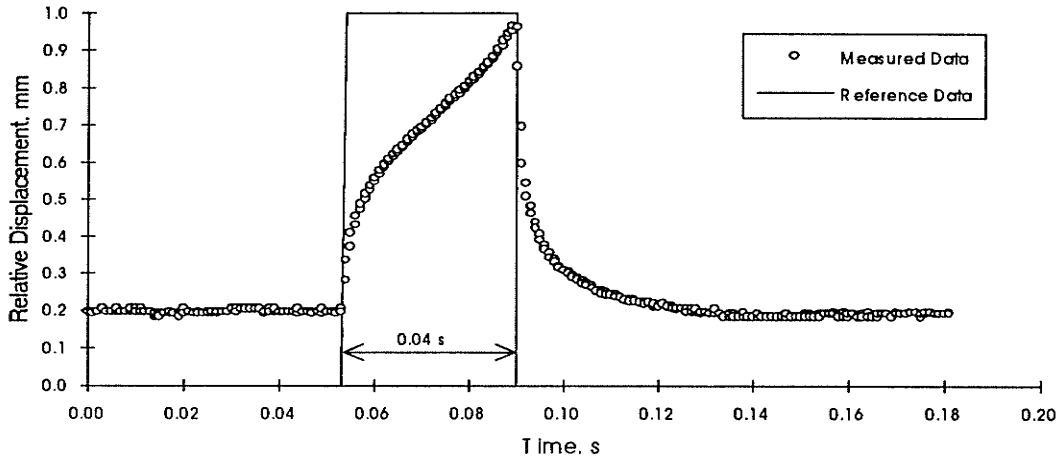

Figure 2.11. Signal Caused by Protrusion.

Furthermore, Figure 2.12 is reconstructed from the difference between two consecutive displacements given in Figure 2.11 to approximate the relative velocity's temporal variation. Figure 2.12 has two distinct peaks that indicate instants when the light is interrupted. These, more easily found instants are used to determine the locations of the gray level changes shown in Figure 2.2. Details are given in Chapter 4.

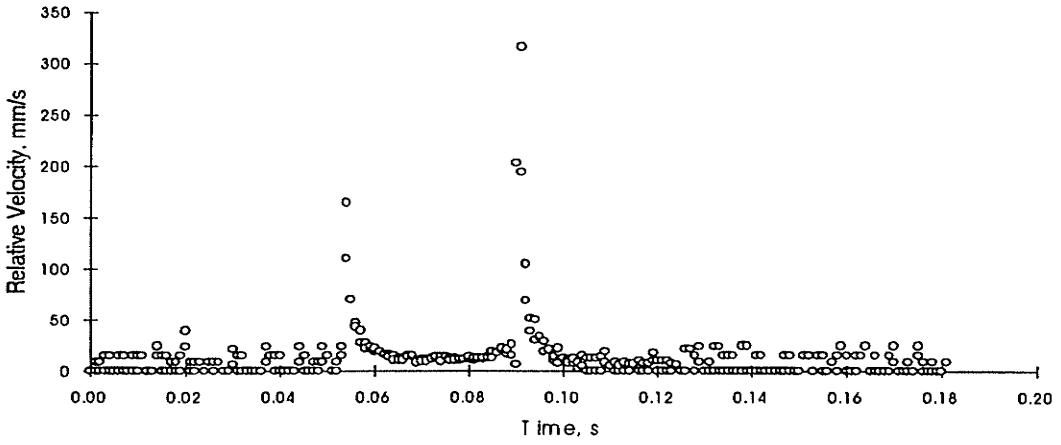

Figure 2.12. Interrupted Signal shown by Sudden Change in Magnitude of Relative Velocity.

CHAPTER 3
ROUGH TURNING

Turning is a machining process in which conical sections are produced by the relative motion between a rotating workpiece and a longitudinally fed, cutting tool. The basic operation for turning a simple cylinder is indicated in Figure 3.1.

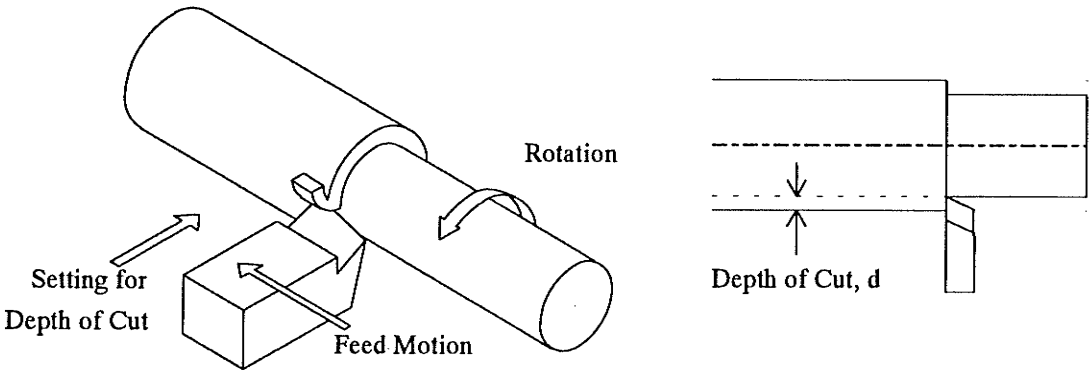

Figure 3.1. Elements of Cutting in Turning.

The spinning of a workpiece, setting the depth of cut, and the feed motion along the workpiece are the three major movements in this operation. These actions are provided by a machine tool called a lathe whose major components are depicted in Figure 3.2. A chuck is a clamping device that is used to hold and spin a workpiece. The workpiece is supported at its other end by the tailstock in order to have a firm and stable spinning motion for cutting. A cutting tool is held by a tool post which can be moved along (feed motion) and across (changing depth of cut) the spinning center. The respective axes for these traveling directions are conventionally set to be the Z-axis and X-axis, respectively.

Most turning is rough cutting followed by finish cutting to bring a workpiece to the desired size and finish. In rough turning, a larger depth of cut and a smaller feedrate are usually preferred compared to those employed in finishing. However, the selection of the cutting parameters depends upon the lathe's capacity as well as a workpiece's surface

condition. The goal in rough turning is to bring a workpiece close to its final dimension as quickly as possible. Unlike rough turning, finish turning is light, with the depth of cut usually set to less than 0.381 mm (0.015"), whilst the feed is as fine as necessary to give the desired finish. A partially automated finishing process employing laser measurements has been reported already [1-5], so that only a complementary but completely automated approach to rough cutting is studied here.

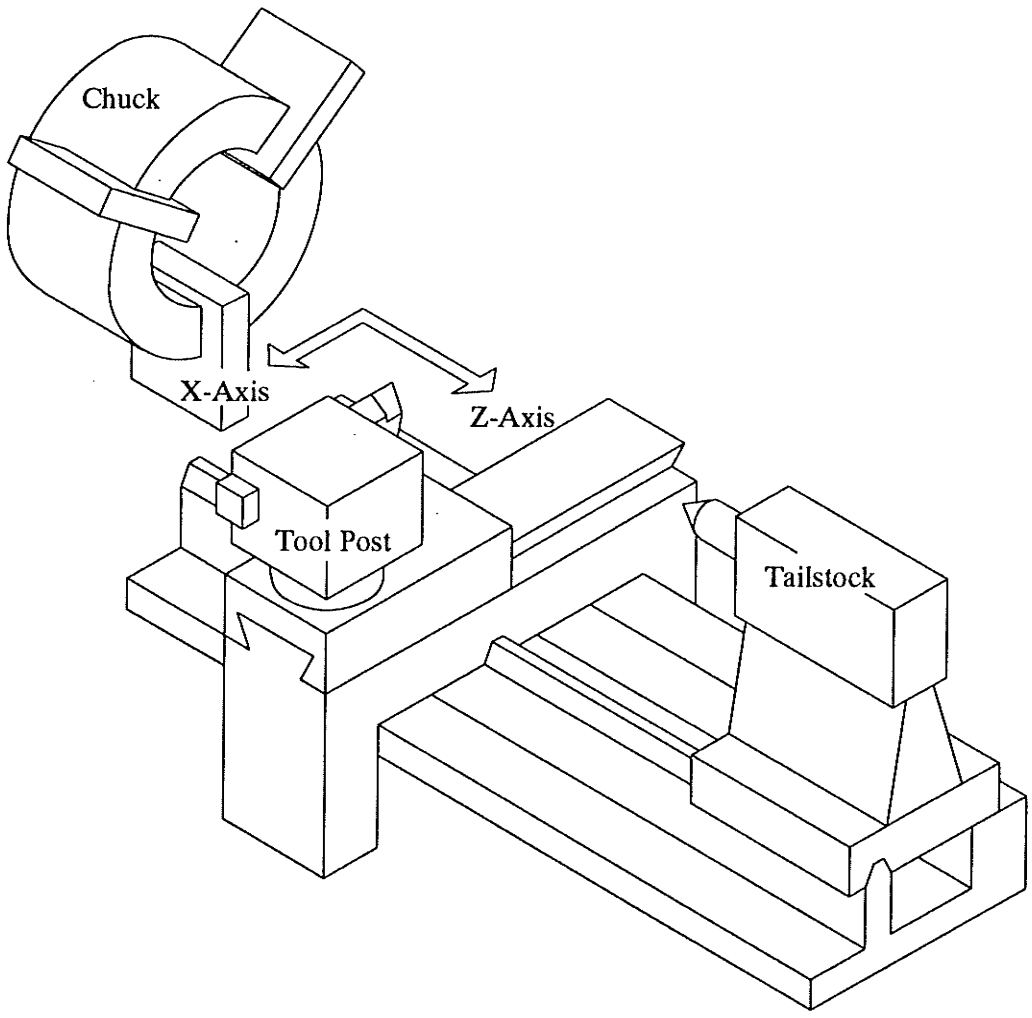

Figure 3.2. The Major Components of a Lathe.

3.1 Selection of Cutting Parameters in Rough Turning

The objective in rough turning is to maximize the material removal rate (MRR) which can be described by [8].

$$MRR = d \times f_r \times V_c \tag{3.1}$$

where d = depth of cut, mm

f_r = feedrate, mm/rev

V_c = cutting speed, m/min.

The three variables at the right side of equation (3.1) represent the control parameters in rough turning. Enlarging any one or all of these parameters will increase the MRR but limitations to this procedure always exist. Although the parameters can be determined from a look-up table in a reference metal cutting handbook [8], these values only provide a guideline for certain cutting conditions. An extra calculation is normally required to interpolate a desired cutting condition between two reference data. Therefore, a computer program and computer data files are created to serve as an automatic data retrieval and calculation system. Such a system provides quick access to the cutting parameters for commonly used metals, such as steel, aluminum, and copper. Parameters that have been extracted from [8] for cutting a low carbon steel with a high speed, steel cutting tool are reproduced in Table 3.1 for illustration purposes. As the goal in rough turning is to maximize the MRR, the combination of cutting parameters that provides the maximum MRR should be chosen. This maximum corresponds to the cutting conditions given in the last row of Table 3.1. However, heavy cutting requires a motor having more horsepower than that in light cutting. Therefore, the motor power of a lathe must be considered when selecting the depth of cut.

Calculated MRR (cm^3/min)	Depth of cut (mm)	Feed (mm/rev)	Cutting speed (m/min)
11	1	0.18	60
72	4	0.40	45
148	8	0.50	37
324	16	0.75	27

Table 3.1. Traditional Cutting Parameters for Low Carbon Steel and a High Speed Steel Tool [8].

3.1.1 Required Motor Power for Cutting

The motor power required for a large depth of cut is calculated from [8].

$$KW_m = \frac{MRR \times P}{E} \tag{3.2}$$

where KW_m = power of motor, kW

P = unit power, kW/cm^3/min

E = efficiency of spindle drive.

For example, the motor power required for the cutting parameters shown in the last row of Table 3.1 is 23.9 kW. This calculation is based upon the reasonable assumption of 80 % efficiency at the spindle drive and a 0.059 unit power. The unit power, P, is a function of empirical data which depends upon the workpiece's hardness and the tool's material. These values can be found from Tables 17.2-17.4 of reference 8. However, the lathe used provides only 1.4 kW which is far less than the 23.9 kW motor power required for the 16 mm depth of cut suggested by Table 3.1. Therefore, to select the maximum permissible depth of cut and the corresponding cutting speed and feedrate, interpolation is needed between the reference data.

3.1.2 Estimation of Maximum Permissible Depth of Cut

The depth of cut in rough turning a usually hard surface, such as a cast or hot-rolled material containing mill scale, should be sufficiently deep to penetrate the hardened material. Otherwise, the cutting tool's entire edge operates in a hard and abrasive material and it will dull rapidly. Although the present work assumes uniform material properties, this assumption is valid only for workpieces having a small cross-section because the depth of cut is normally sufficiently high to penetrate the layer of abrasive material. Furthermore, a previously scrapped workpiece usually has had this abrasive layer removed. Therefore, a depth of cut that is selected purely on the maximum motor power available to the lathe used in this work is usually adequate.

The selection of a depth of cut is an iterative process. First, a value is chosen arbitrarily within the upper and lower limits of a reference depth. Then two reference values are selected that are closest to the arbitrarily picked values. The corresponding feedrates and cutting speeds are also selected by linear interpolation. For example, the linearly interpolated feedrate and cutting speed for a 1.5 mm depth of cut are listed in Table 3.2 where the reference data is given for 1 mm and 4 mm cuts [8].

Depth of cut (mm)	**Feedrate (mm/rev)**	**Cutting speed (m/min)**
1	0.18	60
1.5	*0.22*	*58*
4	0.40	45

Table 3.2. Interpolated Feed and Cutting Speed for a 1.5 mm Cutting Depth.

The motor power is calculated by substituting the interpolated values into equations (3.1) and (3.2). If the resulting motor power is higher than the lathe's actual power, then the assumed depth of cut should be decreased, otherwise it is increased. A new depth of cut

should be assigned for recalculating the feed and cutting speeds. This procedure is repeated until the calculated motor power is slightly below or equal to the actual motor power. After several iterations, the calculated power for a 1.5 mm depth of cut is found to be 1.4 kW which matches the lathe's actual power. Therefore, a depth of cut of 1.5 mm, a feed of 0.22 mm/rev, and a cutting speed of 58 m/min are selected.

3.2 Determination of Tool Cutting Sequence

For a workpiece like a cylinder which has a constant diameter, the cutting tool cuts from right to left (for a standard right hand tool) after setting a suitable depth of cut. However, in the rough turning of an arbitrarily shaped workpiece, a modification of this simple cutting sequence may result in a beneficial time saving. This modification depends upon the workpiece's spinning profile so the profile should be mapped first. Consequently, an irregularly shaped workpiece may have to be cut manually because the determination of an irregular profile requires human vision. Moreover, the selection of a cutting sequence also requires experience. Therefore, to fully automate the cutting process, a lathe must be equipped with a vision system and the tool controller must have the capability to determine the cutting sequence.

Modification of a cutting sequence can benefit the MRR in turning an arbitrarily shaped workpiece. The spinning profile of an arbitrary workpiece and its dimensions are shown in Figure 3.3. Because the profile is symmetrical about its rotational center, only the upper portion of the profile is illustrated. Subsequently, the workpiece and tool material are assumed to be low carbon steel and high speed steel, respectively, so that the cutting parameters obtained in Section 3.2 can be used again. The workpiece (which has a 15 mm maximum cross-sectional radius) is to be turned, for illustrative purposes, to a cylinder having a radius of 10 mm.

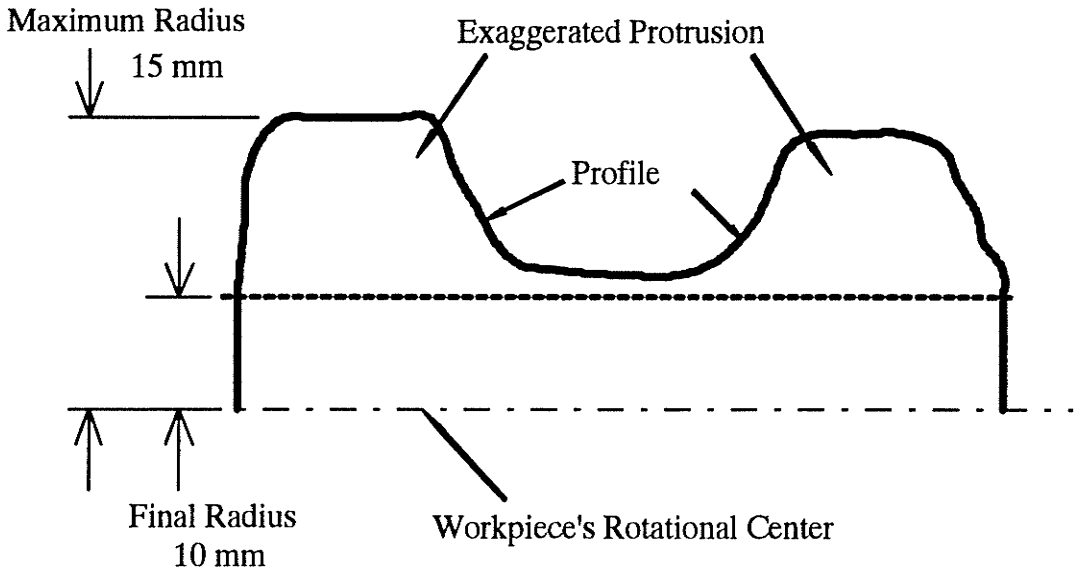

Figure 3.3. Upper Portion of a Symmetrical Profile.

3.2.1 Conventional Cutting

Conventional cutting is the simplest strategy because once all the cutting parameters are selected, they remain unchanged. The depth of cut is adjusted according to the maximum value calculated. The cutting sequence is repeated from right to left, under the constraint of using a standard right hand tool, and the tool returns to its starting location after each layer of material is removed. The start and end locations of the tool are controlled by the extreme right position of the workpiece and the final length of the workpiece, respectively. Details of the tool's cutting sequence and locations for an arbitrary workpiece are shown in Figure 3.4. The cutting path is represented by dotted lines and the arrows show the cutting tool's direction of travel. Furthermore, the heavily dotted lines represent the feed direction and the lightly dotted lines give the direction of the return feed. (These representations of the cutting paths are used throughout.) In conventional cutting, time is wasted when the tool is not cutting during the feed motion.

This situation can be improved by introducing a modified cutting strategy which simply speeds up the tool's motion when no material is being cut.

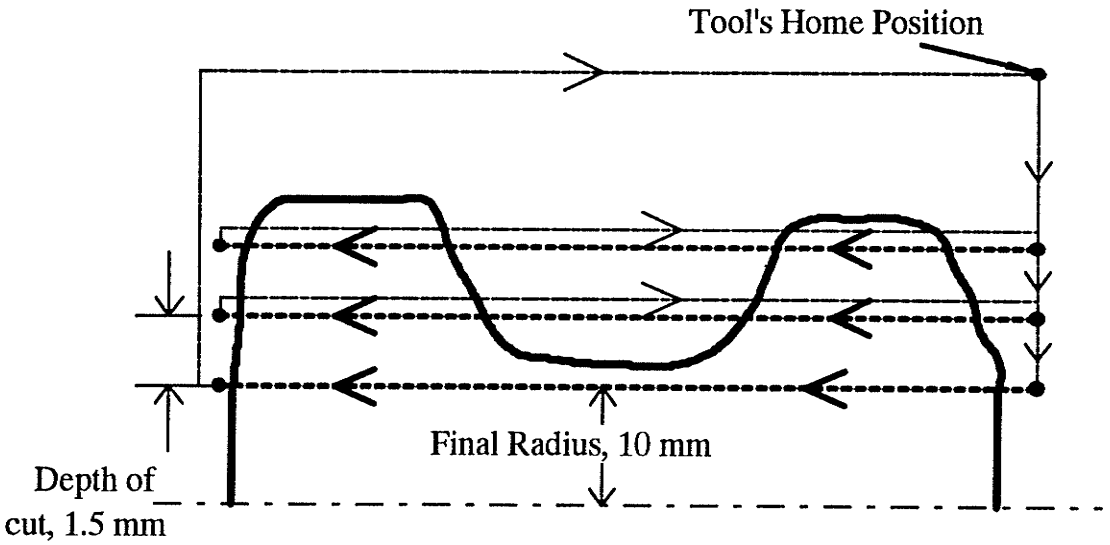

Figure 3.4. Tool Path for Conventional Cutting.

3.2.2 New Heuristic Approach to Cutting

The new cutting strategy is a combination of feedrate compensation and tool relocation. Other cutting parameters are selected automatically from a conventional but computerized base of cutting data. Feedrate compensation involves increasing the feedrate when no material is removed. A heuristic approach is shown to create the optimal tool relocation sequence for a prescanned workpiece. The profile shown previously in Figure 3.3 is used to illustrate the relocating sequence of the tool. Before determining the relocating sequence, however, the layout of the start and end cutting locations should be known. This is accomplished by the following procedures. The cross-sectional profile is divided first into 1 mm x 1.5 mm rectangles, where 1 mm represents the slicing width and 1.5 mm indicates the calculated maximum depth of cut. Then the corners of each rectangle that lie just outside the left or right of the profile can be marked as the locations of tool, as shown in Figure 3.5. The tool is moved over these destined locations in such a way that all the protrusions are removed from right to left. Then a final

cut is performed so that the workpiece's radius meets the final radius. The resulting tool path of the heuristic approach is given in Figure 3.6.

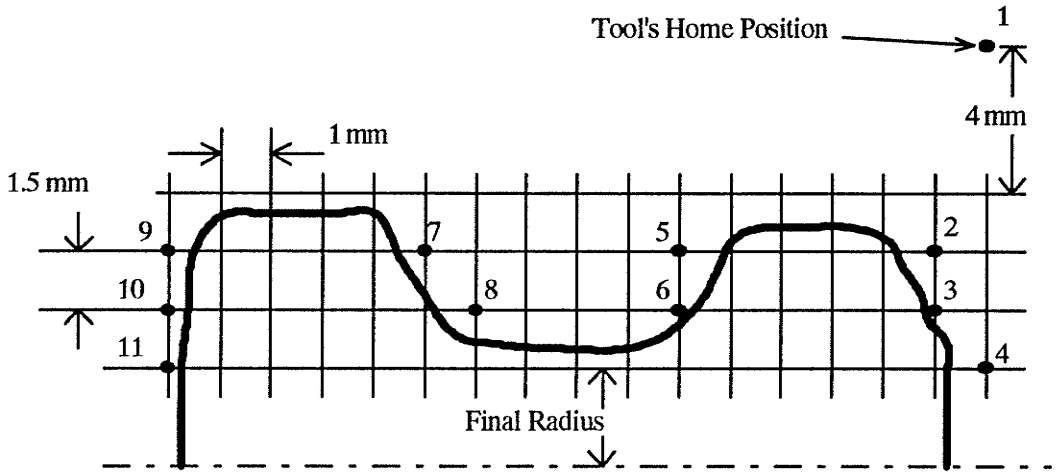

Figure 3.5. Profile Grid and Numbered Tool Locations.

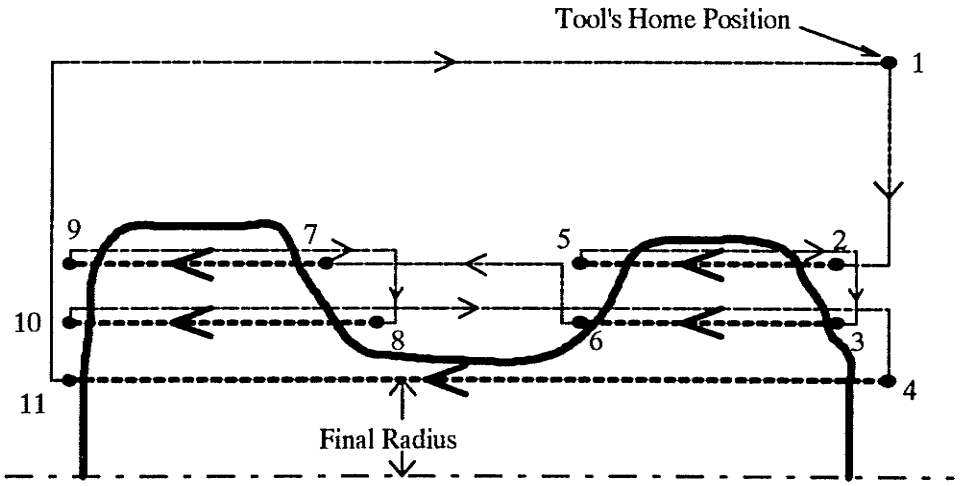

Figure 3.6. Tool Path Determined Heuristically.

3.2.3 Validation of New Strategy

The branch-and-bound approach for the standard traveling salesman problem [21] is adopted to demonstrate that the heuristic approach can provide an optimum relocation sequence for the cutting tool. The branch-and-bound approach is used to solve an illustrative problem by utilizing a zero or one integer programming technique implemented in software called LINDO. The objective of the travelling salesman problem is to determine the travelling sequence around pre-selected cities that produces the shortest travel time. The determination of the optimum relocation sequence for the cutting tool can be tackled by using the same technique.

The profile shown in Figure 3.3 is used again as an example in which the same tool locations as before are employed. The next step is to form a travelling time matrix, T_{ij}, between two tool locations, i and j, for all possible combinations of locations. A variable, X_{ij}, having a value of either zero or one is assigned to each i to j travel segment to indicate the selection result. If X_{ij} is one, then a tool must travel from node i to node j, otherwise the tool does not travel along that segment.

The time spent traveling from node i to node j, T_{ij}, can be calculated by using [8],

$$T_{ij} = \frac{D_{ij} \times D_t \times 60 \times \pi}{f_r \times V_c \times 1000} \tag{3.3}$$

where D_{ij} = distance, in mm, between nodes i and j,

D_t = maximum diameter, in mm, of workpiece.

For example, the time required for the tool to remove material at a 0.22 mm/rev feedrate between nodes 2 and 5 shown in Figure 3.5 is $\frac{5 \times 30 \times 60 \times \pi}{0.22 \times 58 \times 1000} = 2.22$ s. When the tool is merely relocated to another position without cutting occurring, the feedrate (called the relocating feed) can be set to the highest feedrate of 1 mm/rev provided by the machine

used in this study. Hence, the time spent in relocating a tool from node 5 to node 7 is $\frac{5\times 30\times 60\times \pi}{1\times 58\times 1000}$ = 0.49 s. When i equals j, T_{ij} is set to an arbitrarily large positive integer to prevent the tool from travelling between identical locations. All the calculated values for T_{ij} are listed, in s, in Table 3.3.

T_{ij}	j=1	2	3	4	5	6	7	8	9	10	11
i=1	999	0.63	0.78	0.83	1.12	1.27	1.61	1.66	2.10	2.24	2.39
2	0.63	999	0.15	0.39	2.22	2.37	2.71	2.76	4.93	5.08	5.23
3	0.78	0.15	999	0.24	2.37	2.22	2.86	2.61	5.08	5.27	5.42
4	0.83	0.39	0.24	999	2.61	2.46	3.10	2.85	5.32	5.51	7.09
5	1.12	0.49	0.64	0.88	999	0.15	0.49	0.54	2.69	2.84	2.99
6	1.27	0.63	0.49	0.73	0.15	999	0.63	0.39	2.85	3.05	3.2
7	1.61	0.98	1.12	1.36	0.49	0.64	999	0.24	2.22	2.37	2.52
8	1.66	1.02	0.88	1.12	0.54	0.39	0.24	999	2.46	2.66	2.81
9	2.10	1.46	1.61	1.85	0.97	1.12	0.49	0.73	999	0.15	0.30
10	2.24	1.61	1.46	1.71	1.12	0.97	0.63	0.58	0.15	999	0.15
11	2.39	1.75	1.61	1.56	1.27	1.12	0.79	0.73	0.30	0.15	999

Table 3.3. Time Matrix for Tool Locations.

The next step formulates the required mathematical and constraint equations. The tool's total travel time is $\Sigma(T_{ij}\times X_{ij})$ for all i and j nodes when $i\neq j$. The goal is to minimize this time when it is subject to three constraints. First, no tool location can be visited or left more than once so that $\sum_{j=1}^{j} X_{ij} = 1$ for all i, $i\neq j$. Second, the cutting tool must return to its home position after the final cut. Hence, a value of one is assigned to $X_{11,1}$. Third, travel must be unidirectional between two nodes. This requirement can be described

mathematically as $X_{ij}+X_{ji}<=1$ for all i and j, $i \neq j$. Finally, the cutting tool must certainly travel along those path segments where material has to be removed, such as node 2 to node 5, node 3 to node 6, node 7 to node 9, node 8 to node 10, and node 4 to node 11. Therefore, the corresponding values of X_{ij} must be one.

If the result obtained by LINDO shows a tour, then it is the optimal or minimized solution [21]. This means that all tool locations have been visited once within the shortest period because the objective time function $\Sigma(T_{ij} \times X_{ij})$ is minimized. Unfortunately, the optimal solution need not be a tour because it might contain sub-tours. A sub-tour is a round-trip that does not pass through all the required tool locations. The first solution generated by LINDO is shown in Figure 3.7. It can be seen from this figure that two sub-tours are formed that consist of sequences 1-2-5-3-6-4-11-1 and 7-9-8-10-7.

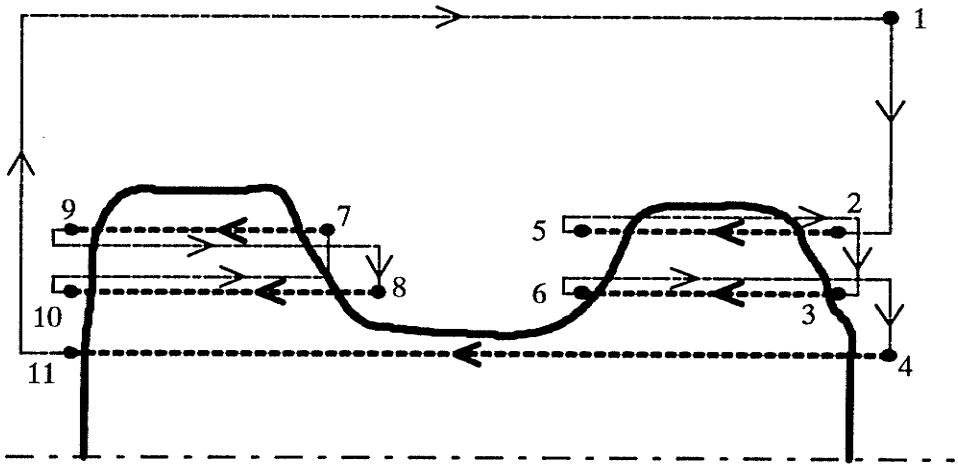

Figure 3.7. First LINDO Solution.

To resolve this problem, the branch-and-bound approach is employed for the traveling salesmen problem [21]. This technique involves the operator inspecting the solution to determine the unfeasible travel segment(s) between any two locations. Such segments are

added as additional constraints. Then the software is rerun and a second solution is obtained. Two unfeasible path segments, comprising node 10 to node 7 and node 6 to node 4, can be observed in Figure 3.7. Two sub-problems can be formed after $X_{10,7}$ and $X_{6,4}$ are set to zero. Hence, two branches are created from the original problem. The same procedures are used to obtain the final solution for both sub-problems. However, for simplicity, only one sub-problem in which $X_{6,4}$ is set to zero is selected for further illustration. If the solution still contains sub-tours, the inspection of unfeasible travel segments must be repeated and the software must be rerun until a feasible tour is formed. Figures 3.8 through 3.11 illustrate the intermediate solutions after certain X_{ij} values are set to zero. After six trials, the optimal solution depicted in Figure 3.12 is obtained because a tour is formed without containing any unfeasible segments. This optimal solution is the same as that found by the heuristic approach. Because the systematic approach is time consuming due to the requirement for operator inspections, the heuristic approach is used here to determine appropriate cutting sequences.

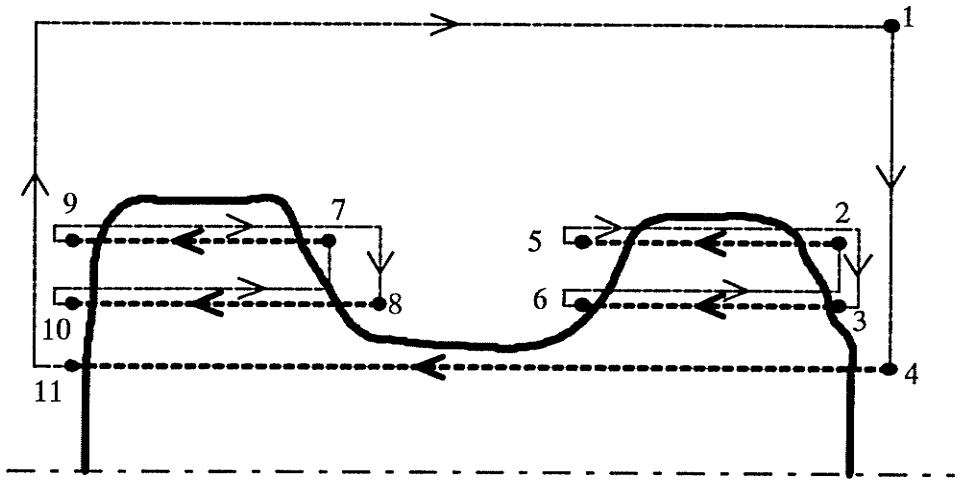

Figure 3.8. Second Solution Adding $X_{6,4}=0$ into the Constraints.

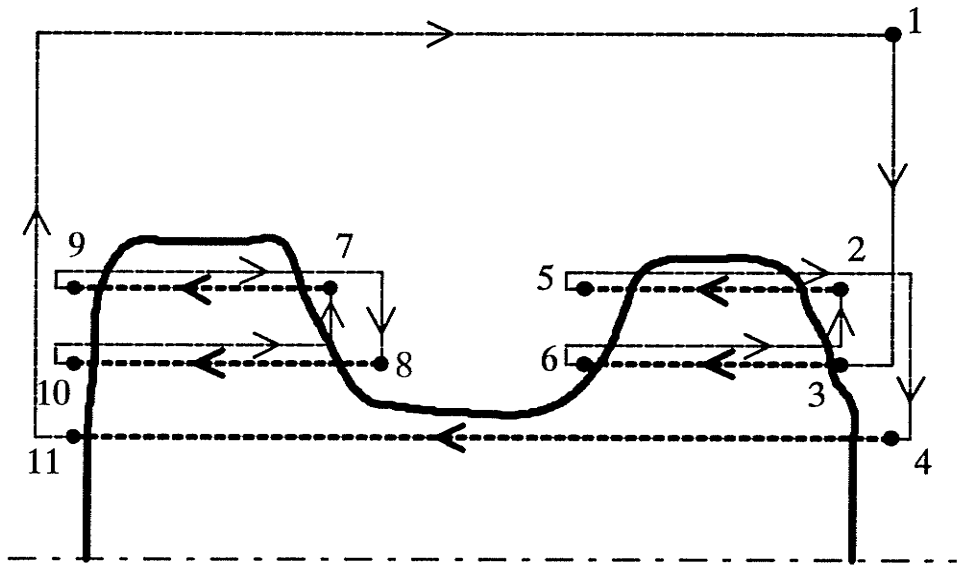

Figure 3.9. Third Solution Adding $X_{1,4}=0$ into the Constraints.

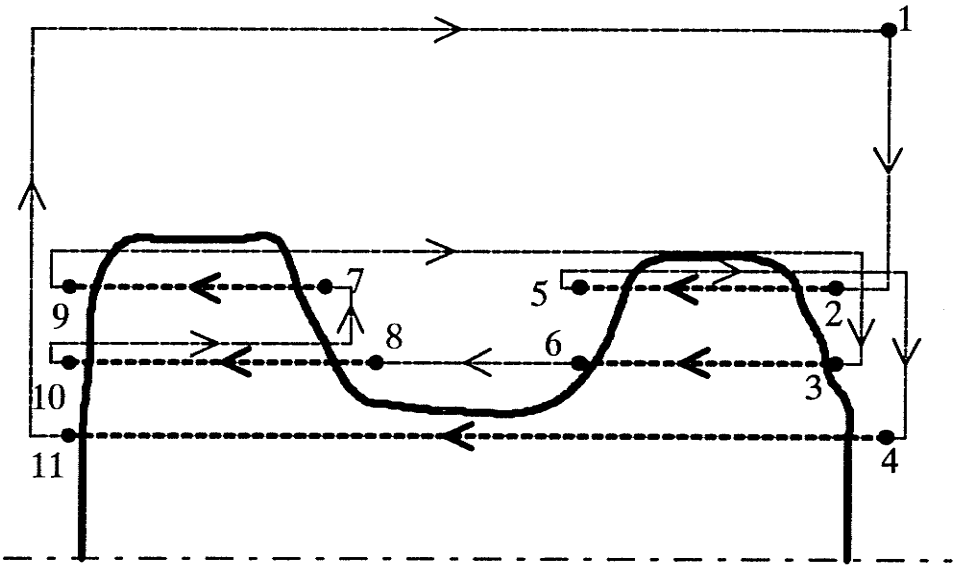

Figure 3.10. Fourth Solution Adding $X_{1,3}=0$ into the Constraints.

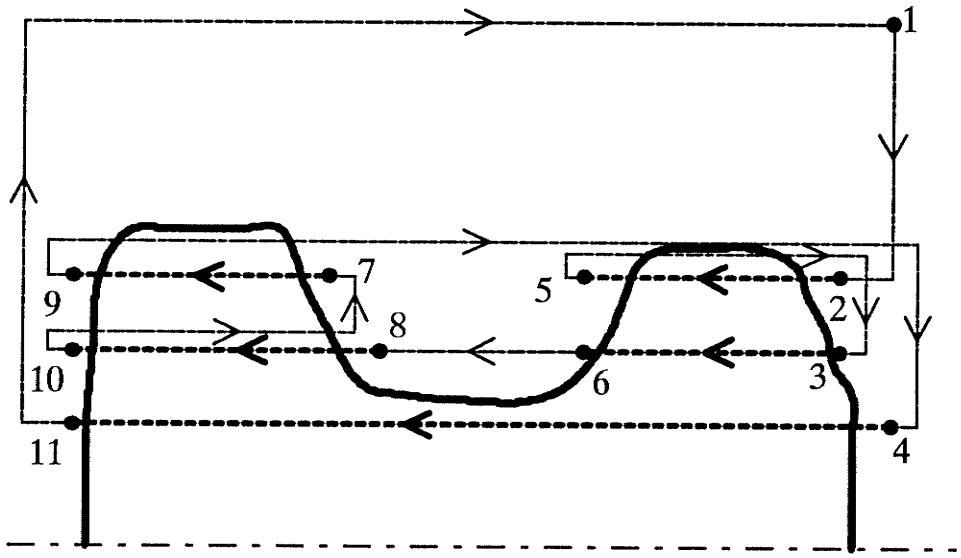

Figure 3.11. Fifth Solution Adding $X_{5,4}=0$ into the Constraints.

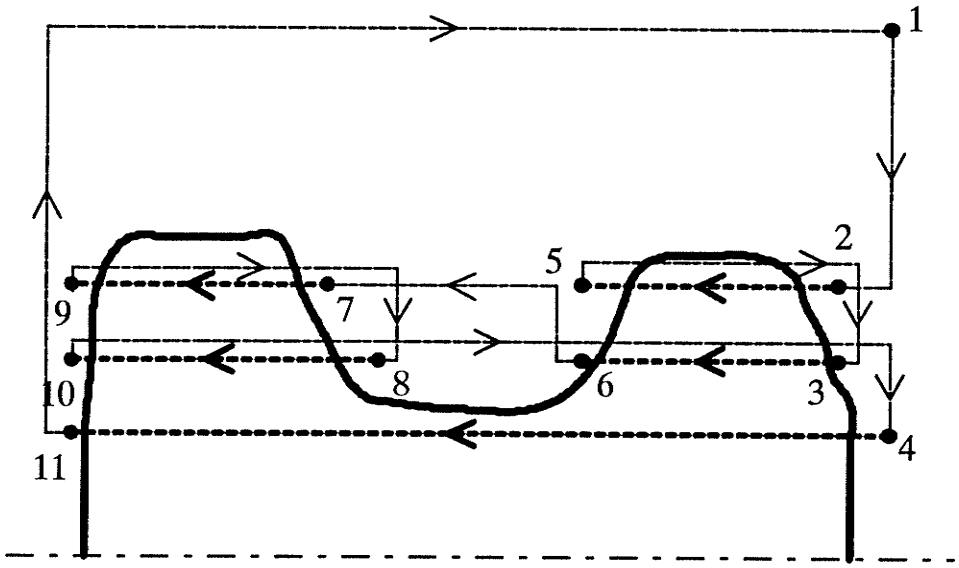

Figure 3.12. Optimal Solution.

3.2.4 Example of Time Saving from the New Cutting Strategy

Time spent in conventionally cutting the profile illustrated in Figure 3.4 is the sum of the cutting time and the tool's relocation time. Three cuts of 16 mm are required to bring the workpiece to the final size. The cutting time for a feedrate of 0.22 mm/rev and a cutting speed of 58 m/min is three times $\frac{16\times 30\times 60\times \pi}{0.22\times 58\times 1000}$ = 21.27 s. The time spent in relocating the tool during a total travel distance of 65 mm is $\frac{65\times 30\times 60\times \pi}{1\times 58\times 1000}$ = 6.33 s. Therefore, the total time spent for conventional cutting is (21.27 + 6.33) = 27.70 s.

The optimal tool relocation sequence is 1-2-5-3-6-7-9-8-10-4-11-1. The total cutting time of 23.14 s can be obtained by adding the time spent on each of the traveling segments listed in Table 3.3. Therefore, the new strategy reduces the cutting time by $\left(\frac{27.70-23.14}{27.70}\right)\times 100\% = 16.5\%$.

CHAPTER 4
EXPERIMENTS AND RESULTS

The principle and mechanism of the new measurement device, which is used to map spinning profiles of a rigid workpiece and monitor the vibration caused by the cutting process, were discussed in Chapter 2. Two experiments were also conducted to determine the characteristics of the sensor. They indicated that the sensor was sensitive to intermittent changes in light intensity. Therefore, a prototype was designed and built. The prototype was also used as a vibration detector. By monitoring and comparing the vibration signal with a reference signal, the depth of cut was adjusted to ensure that the vibration magnitude remained "normal". In the case of tool breakage, a sudden change would occur in the magnitude of the relative displacement between the laser's spot and the sensor's pin hole. Consequently, the prototype was able to detect tool breakage. Furthermore, a new cutting strategy improved the MRR, especially for a workpiece having irregular profiles. The following sections detail the experimental setup and the ensuing results.

4.1 Hardware

The experimental system, which included the prototype and a computer controlled EMCO lathe, was installed at the Computer Integrated Manufacturing and Automation Laboratory in the University of Manitoba. A schematic of the system is shown in Figure 4.1. The spindle speed of the lathe could be selected manually by using an eight-speed gearbox. The spindle power was supplied by a three-phase, 1.4 kW motor. The original, open loop mechanism controlling the feedrate along the Z-axis and the tool's depth of cut along the X-axis were disconnected and replaced by two Electrocraft servo motors. Each servo motor was equipped with a tachometer and an optical encoder which were connected to the motor's drive shaft for velocity and position feedback, respectively.

[23]. A Techmar Scientific Solution CY-525 stepper motor controller card was responsible for the communication between the stepper motor and the microcomputer. It was a programmable peripheral controller card that could be used to store an instruction sequence for routine control, so that the main control program could be simplified. Besides, the oscillating motion of the mirror and the slicing motion of the arm required only routine control. Hence, the CY-525 stepper motor controller card was selected. Finally, the sensor's output voltage was digitized by employing a DASH-16G analog to digital (AD) converter. It was a 12-bit converter having a resolution of 0.002 V in the signal's conversion of a d.c. voltage from 0 to 10 V, and the sampling rate could be set as high as 10 MHz. Therefore, it provided acceptable data acquisition for the present studies.

4.2 Profile Mapping

After the prototype was attached to the lathe, the locations of the laser, arm and mirrors were configured in the following manner. First, the laser's location was adjusted to provide a laser beam which was absolutely parallel to the chuck's axis of rotation. Second, the re-orientation mirror was tuned to $45.0^{\circ} \pm 0.1^{\circ}$ relative to the incident laser beam. The laser beam then reflected from the oscillating mirror and hit the sensor's pin hole after the final adjustment of the locations of the oscillating mirror and arm. The acute angle of $32.5^{\circ} \pm 0.5^{\circ}$ formed between the reflecting surface of the oscillating mirror and the negative Y-axis, which had an origin at the oscillating mirror's center of rotation, was selected. Consequently, the initial position of the arm was located such that a 25° angle was formed between the reflected laser beam from the oscillating mirror and the negative Y-axis. This initial 25° angle was selected to cover a workpiece diameter varying from 10 mm to 100 mm. Finally, the lower arm was adjusted to ensure that the reflected laser beam precisely hit the sensor's pin hole. The resulting configuration of the arm is shown in Figure 4.2(a) where it is named position (1). After all these adjustments were performed,

the arm was programmed to move within a span of 30°. Then the resulting slicing motion ensured that the laser beam was blocked by the rotating workpiece during the arm's motion without a collision occurring. The following sections explain how the prototype was used to obtain the particular image locations numbered 1 and 2 in Figure 2.2 from a spinning profile.

4.2.1 Synchronization of Laser Beam and Sensor

The principle underlying the synchronization of the oscillating mirror and the sensor was explained in Section 2.2. The remainder of this section is used to discuss the test results. In Figure 4.2, various locations of the arm are shown when the arm has been programmed to swing down 30° from its initial position. Corresponding signals are also depicted to illustrate the result of synchronization. The relative displacement presented in Figure 4.2(b) should ideally remain zero – a situation that corresponds to the abscissa of this figure. However, the measured curve has a fluctuation and an offset above the ideal situation. The fluctuation resulted from the arm's vibration due to a sudden acceleration from the initial position (1) of Figure 4.2(a) as well as the imperfectly meshed gears within the prototype's gear train also caused vibration during the motion. The offset was the result of misalignment between the laser beam and sensor due to difficulty in obtaining the perfect arm's initial position. Furthermore, when the arm approached the position (2), the arm's counter clockwise moment about its rotational center decreased because the moment arm's distance (between the Y-axis and the vertical force acting through the arm's center of gravity) was smaller. Consequently, the gears are fully engaged at position (1) but gradually lost their interlock as the arm moved to position (2) because of the changing moment and backlash. Eventually, the backlash influenced the ongoing arm's motion and led to a serious misalignment between the laser beam and sensor. This effect is shown by the second offset after about 1.6 s in Figure 4.2(b). Finally, the arm's vibration faded slowly after the arm stopped in position (3).

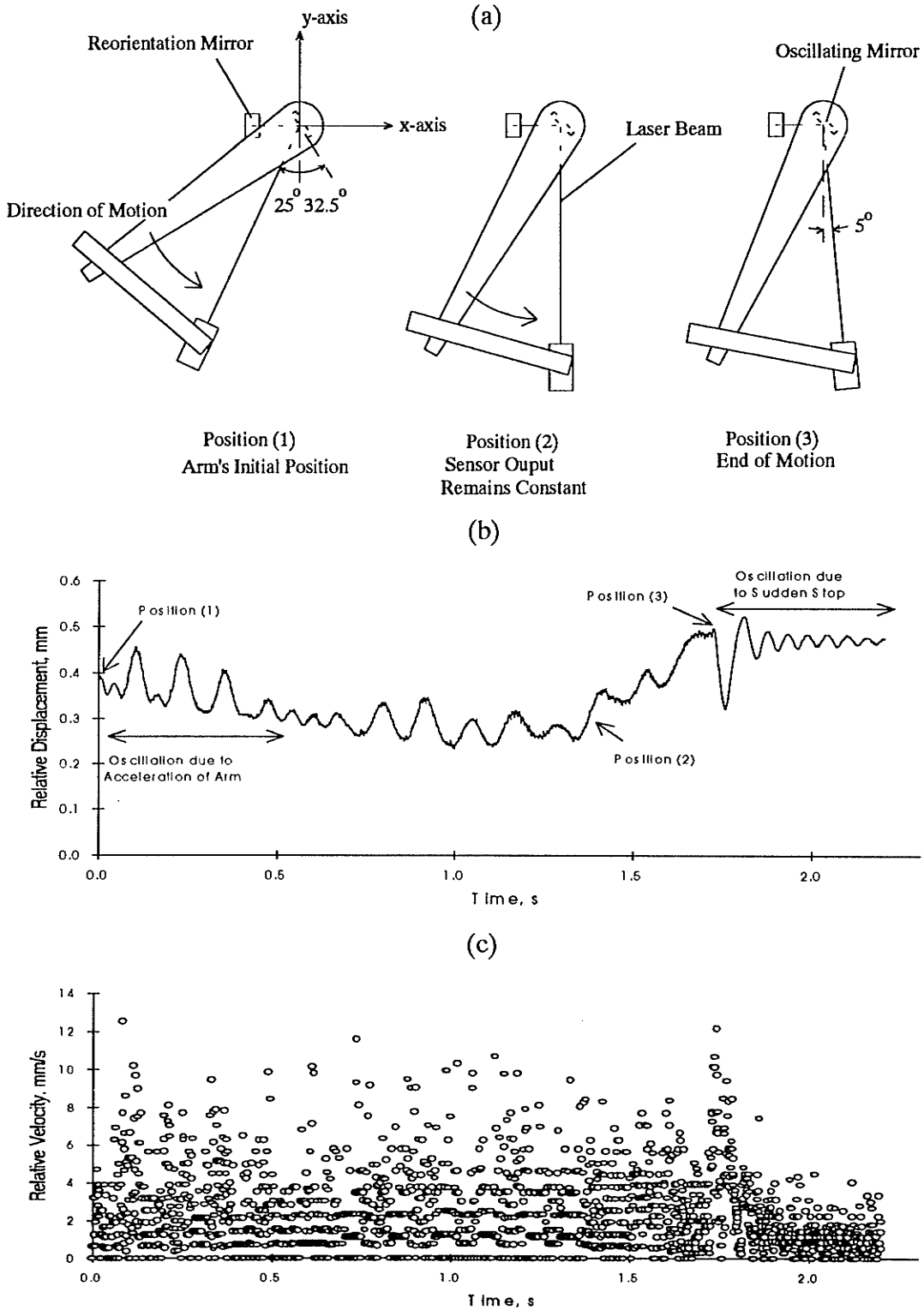

Figure 4.2. Illustrating Synchronization. (a) Locations of Arm, (b) Relative Displacement, and (c) Noise Represented by Relative Velocity.

To reduce the measured offset, the relative displacement of Figure 4.2(b) was replotted in Figure 4.2(c) in terms of the corresponding relative velocity. The simplest difference formula was used between consecutive displacement to approximate the slop. It can be seen from Figure 4.2(c) that the offset has been eliminated but that the fluctuations remain. However, the relative velocity generated during the interruption of the laser beam (see Figure 2.12), had a magnitude around 150 mm/s – a value that is about ten times higher than the noise floor of about 13 mm/s shown in Figure 4.2(c). Thus the relative velocity provided a reasonable basis for reliable profile mapping. Details concerning the selection and use of the threshold velocity are given in the following sections.

4.2.2 Selection of Threshold's Upper Limit

A symmetrical and an asymmetrical workpiece were used to evaluate the upper limit of the threshold's selection. A cylinder was employed to represent a symmetrical workpiece and a cylinder having a simple protrusion mounted on its circumference was used to represent an asymmetrical workpiece. Two kinds of signals were obtained from the prototype device's "slicing" motion. Figures 4.3 and 4.4 show the measurement locations during the arm's motion and the corresponding measurements for the symmetrical and asymmetrical workpieces, respectively. In Figure 4.3(b), a dramatic 0.4 to 1.0 mm change can be observed in the relative displacement at 1.45s. This sudden change indicated that the laser beam was blocked completely by the cylinder, as illustrated at position (3) in Figure 4.3(a). The relative displacement was also converted, as before, into the relative velocity of Figure 4.3(c). It can be seen from the last figure that the maximum allowable velocity threshold should not be greater than the about 27 mm/s observed maximum value. Similar plots are given in Figure 4.4 for the asymmetrical workpiece. However, the sudden change in Figure 4.4(b) from a low to a high relative displacesment at positions(3) and (4), respectively, is preceded by a region containing a

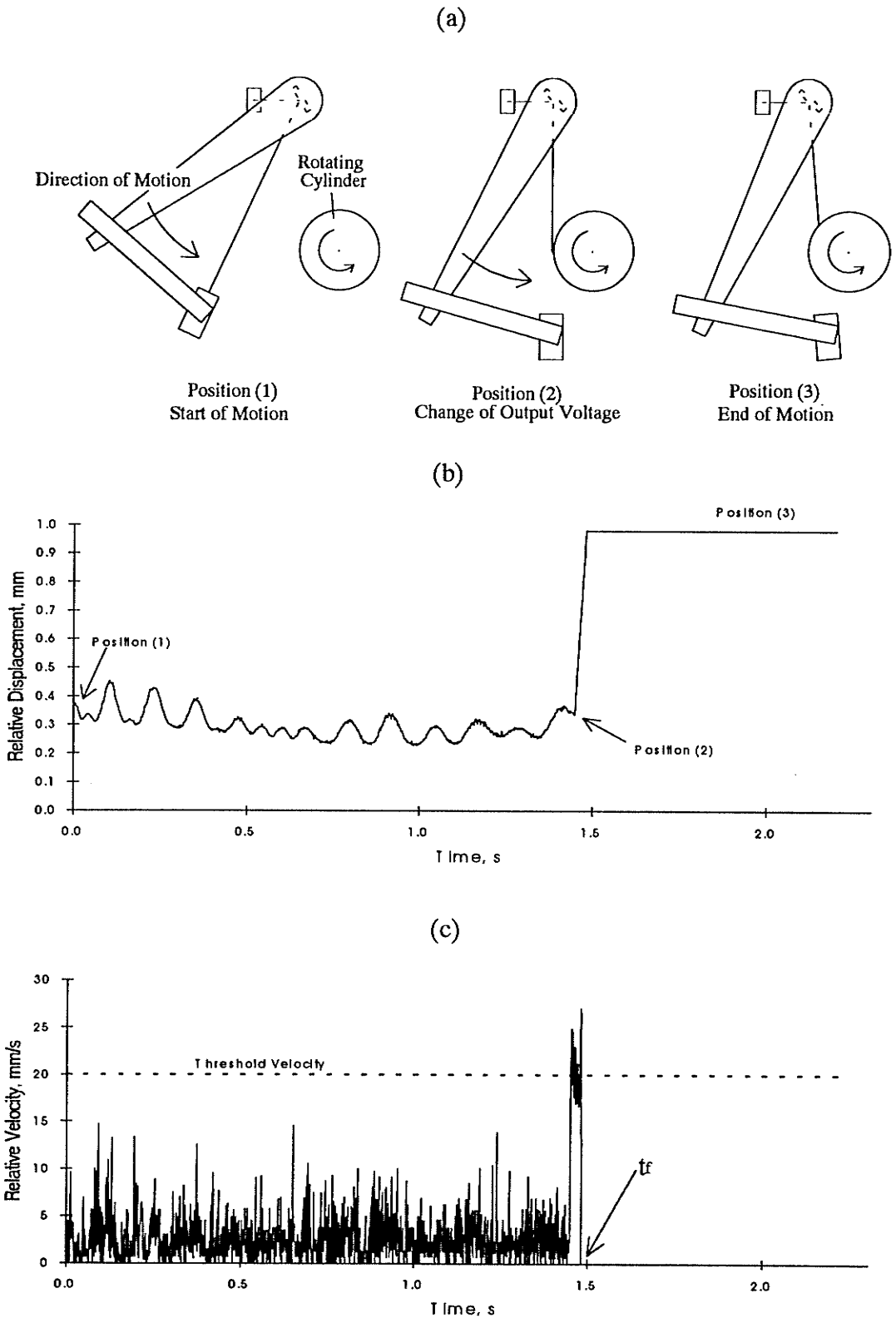

Figure 4.3. Scan of a Cylinder Showing (a) Locations of Arm, (b) Relative Displacement, and (c) Relative Velocity.

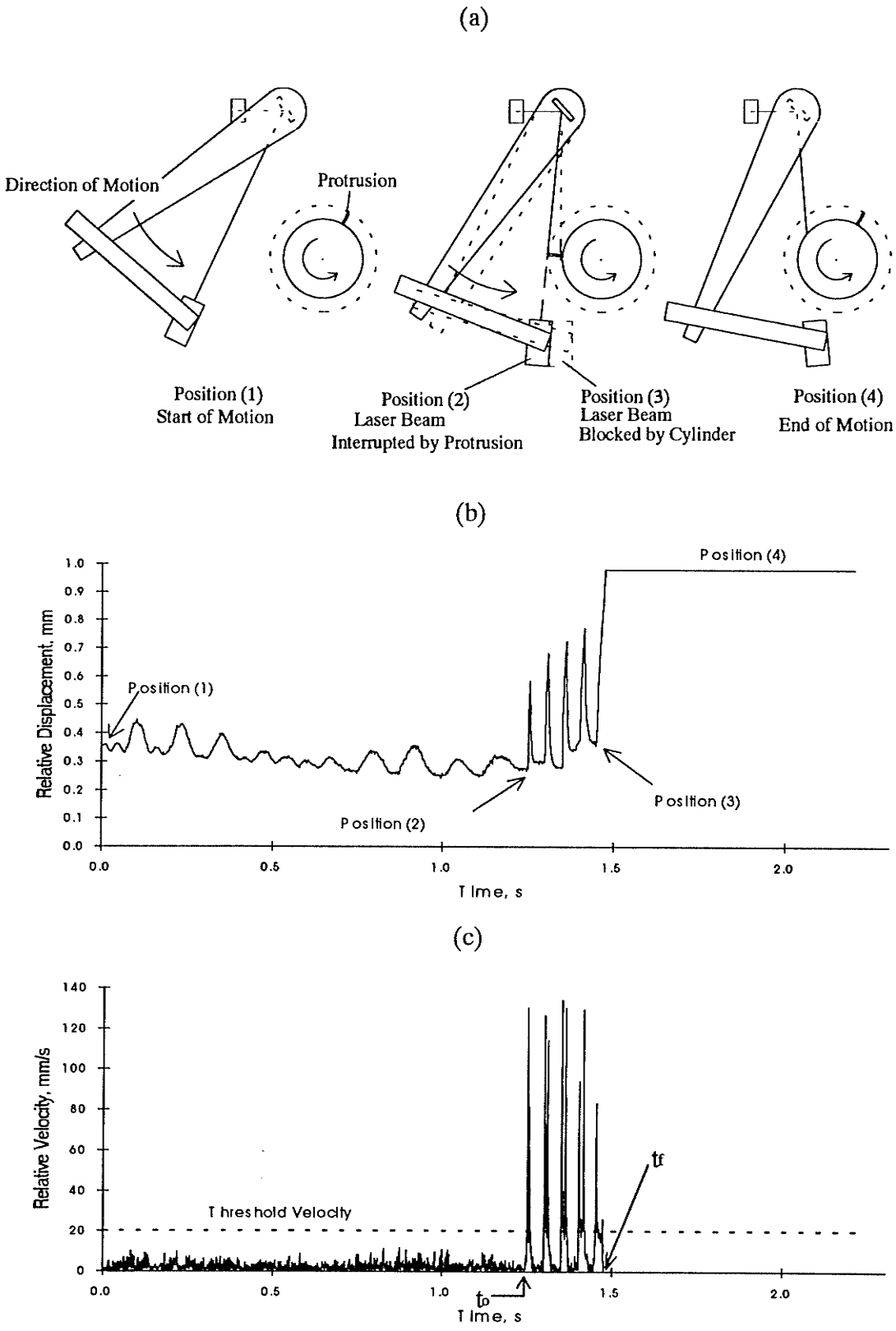

Figure 4.4. Scan of a Cylinder Having a Protrusion and Rotating at 1100 RPM. Showing (a) Locations of Arm, (b) Relative Displacement, and (c) Relative Velocity.

series of gradually increasing peaks. The formation of these peaks is the result of the protrusion interrupting the laser beam which happened between positions (2) and (3). (see Figure 4.4(a).) The magnitudes of these peaks is around 130 mm/s. Nevertheless, to deal with an uncertain type of workpiece, symmetrical or asymmetrical, the higher limit of the threshold value must be selected as the lowest maximum relative velocity between the two cases.

4.2.3 Conversion of Measured Signal into an Equivalent Shaft Diameter

A threshold relative velocity of 20 mm/s was selected because it lies about halfway between the 13 mm/s noise floor and the lower 27 mm/s peak observed for the symmetrical cylinder. This threshold was used to extract the instant, t_o, when the relative velocity first went above the threshold. The later instant, t_f, when the relative velocity invariably became zero was also noted as in Figures 4.4(c). The t_o and t_f correspond to the transition times of the image from bright to light gray and from light gray to dark, respectively. This information was used to obtain the shaft's diameter.

First, however, it should be noted that the experimental configuration was the same as that used to obtain Figure 4.3(a). Seventeen precision made cylinders having diameters from 10.59 ± 0.03 mm to 41.50 ± 0.03 mm were scanned to provide accurate reference diameters. The resulting calibration curve that related a diameter, ϕ_{shaft}, to the blockage duration, t, is given in Figure 4.5. A least square, curve fitting technique [20] was employed to obtain the relationship

$$\phi_{shaft} = -75.09 \times t + 147.30 \qquad (4.1)$$

from this figure. When t_o or t_f is substituted into variable t of equation (4.1), the resulting ϕ_{shaft} is called the inside diameter or outside diameter, respectively.

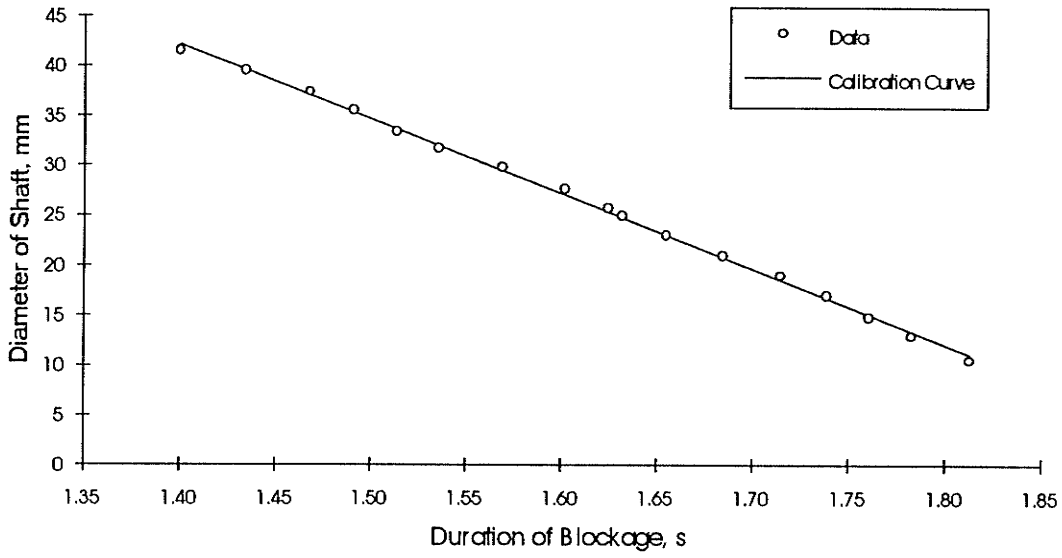

Figure 4.5. Relationship between Duration of Laser Beam's Blockage to a Shaft's Diameter.

The largest variation of the calibration data from this line was 5.4 %. The line was used to extrapolate a dimension that exceeded the largest or smallest diameter in the calibration data. Otherwise, linear interpolation between the two closest data was used to determine an unknown shaft's diameter. Before presenting the results of the profile mapping tests, several factors affecting the performance of the measurement device are mentioned first.

4.3 Factors Affecting the Performance of the Prototype

The rotational speed, $\dot{\theta}$, of an object is same as the sweep speed of the laser beam. The laser's spot size, ϕ_{laser}, and the increment in the distance of the prototype device along the Z-axis, $S_{z\text{-}axis}$, together with $\dot{\theta}$ are the factors that affect the accuracy of the mapped profile. Two kinds of errors have to be considered when evaluating the measurements. First, a non-dimensional error is introduced which is the ratio of the absolute difference between the measured and reference diameters compared to the reference diameter, expressed as a percentage. Second, the Root-mean-square difference, RMS (mm), is used to determine the extent to which a measured profile differs from the reference profile

along a critical region such as a corner or a step. Both errors are presented in conjunction with the measured results in the following sections.

4.3.1 Speed Factors in Measurement Accuracy

The workpiece's rotational speed, RPM, played an important role only in mapping the spinning outside profile because there is no intermittent interruption when the laser beam sweeps through the object's core. Consequently, similar results can be expected when determining the inside diameter at different RPM. This assertion is justified by the scanning results presented in the following section. To obtain an accurate measurement of the outside diameter, however, the laser beam must hit the top of the protrusion and simultaneously form the tangent of the circle generated by the free tip of the protrusion's rotating image. Several possible hitting conditions are illustrated in Figure 4.6.

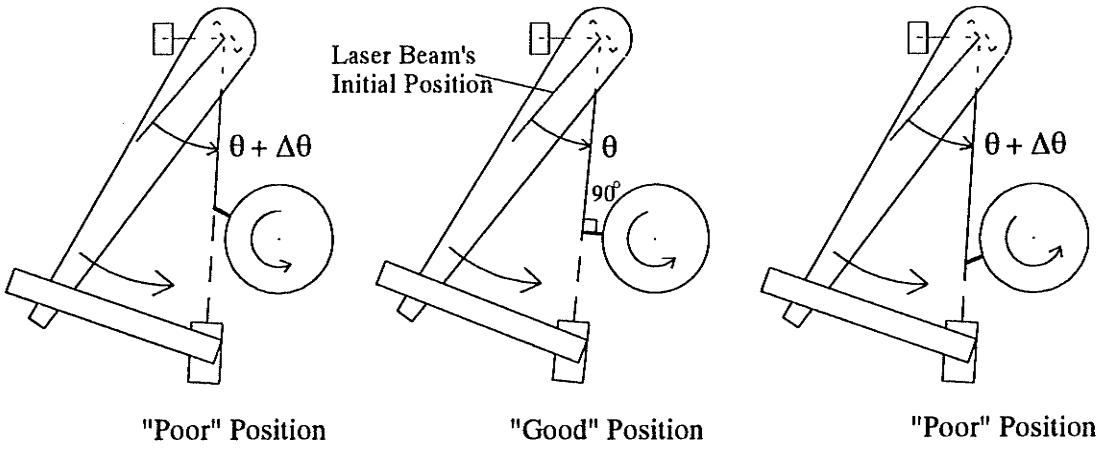

Figure 4.6. Different Initial Contact Positions of Laser Beam and Protrusion.

This figure suggests that the first peak relative velocity does not necessarily coincide with the "good" position. Suppose, for example, the sweep angle from the laser beam's initial position to the "good" position is θ (in rad). Consequently, the sweep angles for "poor" positions are θ+Δθ. Therefore Δθ should be as close as possible to zero in order to improve the situation at the "poor" positions. Δθ can be reduced by adjusting either the

rotational speed or the laser beam's "slicing" speed which corresponds to the angular speed, $\dot{\theta}$, of the arm.

Assume that the "good" position, position (1) in Figure 4.7, is missed as the arm swept through angle θ. Consequently, the first interruption of the laser beam by the protrusion's free end is delayed, Δt, until the protrusion rotates almost one revolution to position (2) in the Figure 4.7. Therefore $\Delta\theta$ is approximately $\dot{\theta} \times \Delta t$. Let R_{error} be the maximum difference between the actual and measured outside diameters. Then R_{error} is approximately the maximum measured radius error which can be calculated from

$$R_{error} \approx \Delta\theta \times L \approx \dot{\theta} \times \Delta t \times L, \tag{4.2}$$

by assuming a small $\Delta\theta$ (rad) and a large L (mm). L is the distance between the arm's center of rotation and the intersection point where the laser beam is tangential to the circular rotating image formed by the rotating protrusion's free end. It can be seen from equation (4.2) that there are three possible ways to minimize R_{error}, but only two of the possibilities are feasible. The first way is to reduce $\dot{\theta}$ the "slicing" speed of arm. However $\dot{\theta}$ cannot be chosen lower than 0.5 rad/s, which is the slowest speed of the present stepper motor. The second way is to reduce Δt. This can be accomplished by increasing the object's rotational speed so that the time taken to complete a revolution is reduced. The maximum possible rotational speed corresponding to the maximum spindle speed of the experimental lathe, that is 2289 RPM or 0.03 s/rev. Hence, Δt must be 0.03 s. The final possibility is to shorten L but this distance is the fixed 28 mm dimension of the measurement device. Therefore, by using equation (4.2), R_{error} must be about $0.5 \times 28 \times 0.03 = 0.4$ mm. This value simply indicates that the most discriminateable in radius is 0.4 mm by using $\dot{\theta} = 0.5$ rad/s and the 2289 RPM.

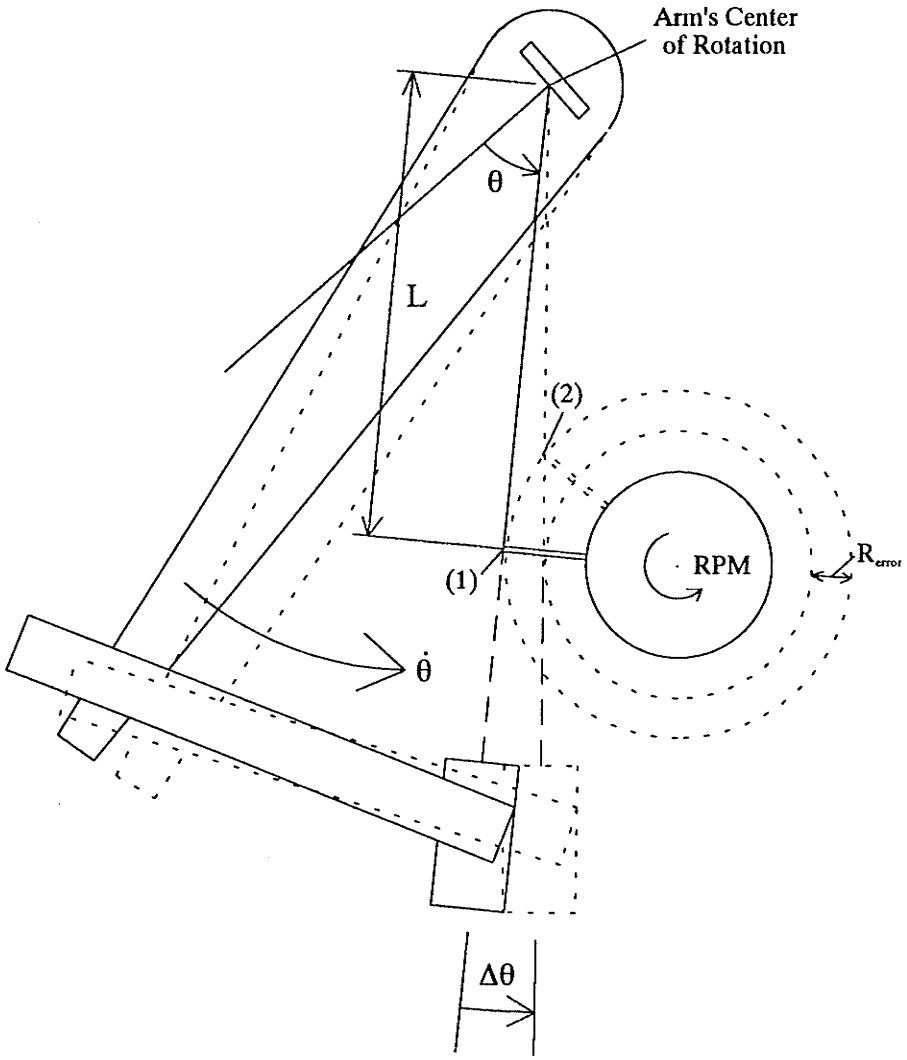

Figure 4.7. Speed Factors Affecting R_{error}.

4.3.1.1 Results at Different Rotational Speeds

A cylinder having a 34.7 mm diameter and a 8.5 mm metal strip mounted on its circumference was used to demonstrate the effect of rotational speed on the accuracy of determining t_o. t_o was used to determine the outside diameter which was the diameter of the circular image formed by the rotating protrusion's free end. The resulting diameter will affect the selection of the cutting tool's minimum starting offset, C_{offset}. (See Figure

2.1.) The cylinder was rotated initially at a constant 200 RPM and subsequently at a constant 2289 RPM. Three sets of readings were recorded. They are plotted in Figures 4.8 and 4.9 to demonstrate differences at the two RPM. The previously discussed (in Sections 4.2.2 and 4.2.3) threshold of 20 mm/s was used to extract t_o. The scanning results are summarized in Table 4.1. As expected, there is no difference in the results for the inside diameters at different RPM. The errors in the outside diameter vary from 4.5 % to 26.7 % at 200 RPM, however, smaller variation of 1.9 % to 4.5 % is observed at 2289 RPM. The difference in the range of variation at different RPM can be explained by using equation (4.2). For instance, 200 and 2289 RPM give Δt of 0.3 and 0.03 s, respectively. Therefore, with the constant $\dot{\theta}$ and L, the most discriminateable variation in radius, R_{error}, at 200 RPM must have a value ten times higher than at 2289 RPM (4.2 mm to 0.4 mm), but the experimental measurement results showed only six times higher. This can be calculated from dividing the $\frac{51.7 - 37.8}{2} = 7$ mm (maximum radius error at 200 RPM) by the $\frac{54.1 - 51.7}{2} = 1.2$ mm (maximum radius error at 2289 RPM). Despite the variation from the measured results, the RPM dependence in the radius measurement was justified.

RPM	Figure	Time, s		Inside diameter, mm			**Outside diameter, mm**		
		t_o	t_f	Actual	Measured	% Error	Actual	Measured	% Error
200	4.8(a)	1.46	1.48	34.7	36.4	4.9	51.7	37.8	**26.7**
200	4.8(b)	1.37	1.48	34.7	36.4	4.9	51.7	44.7	**13.5**
200	4.8(c)	1.24	1.48	34.7	36.4	4.9	51.7	54.1	**4.5**
2289	4.9(a)	1.25	1.48	34.7	36.4	4.9	51.7	53.4	**3.3**
2289	4.9(b)	1.26	1.48	34.7	36.4	4.9	51.7	52.7	**1.9**
2289	4.9(c)	1.24	1.48	34.7	36.4	4.9	51.7	54.1	**4.5**

Table 4.1. Shaft's Diameter Measured at 200 RPM and 2289 RPM.

(a)

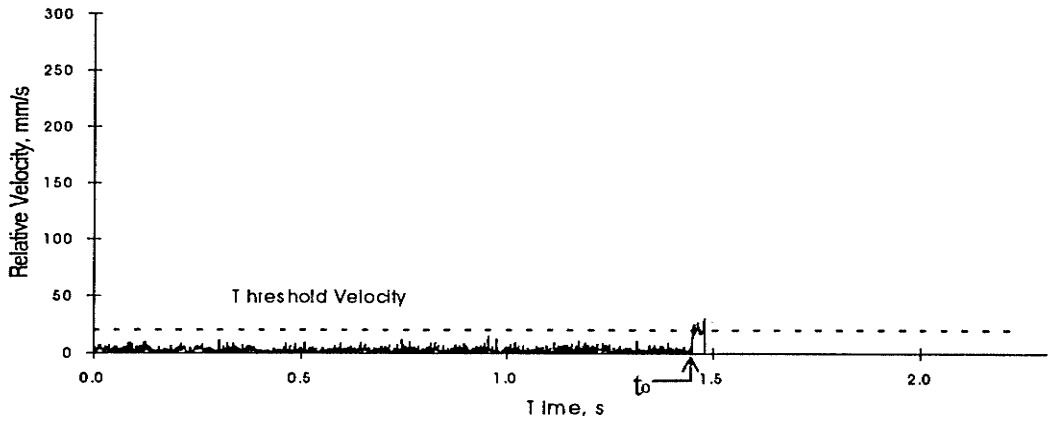

(b)

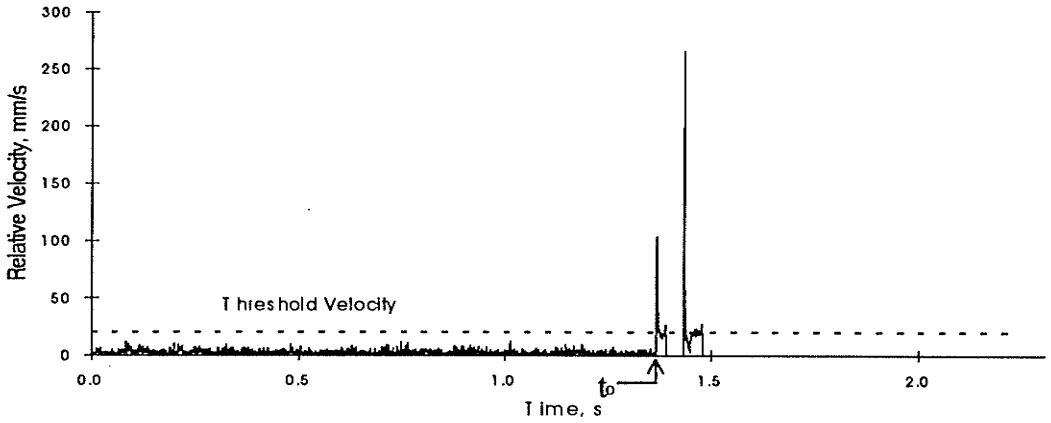

(c)

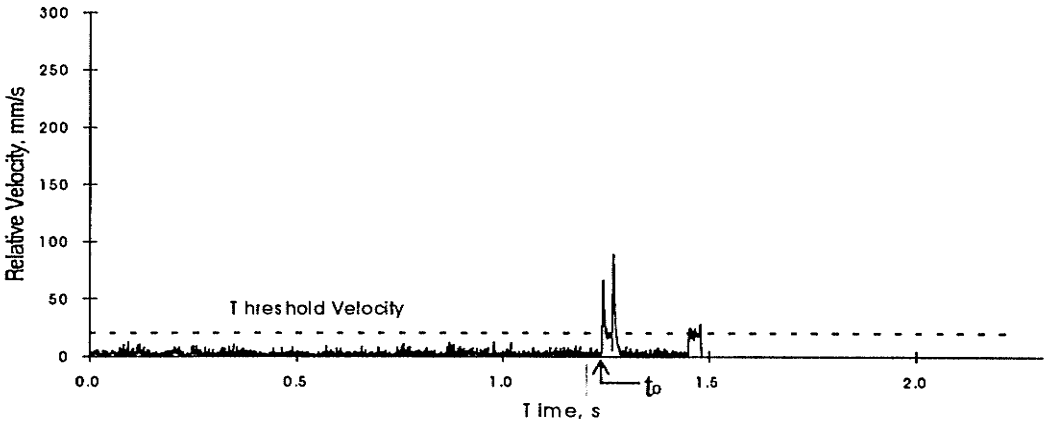

Figure 4.8. A Comparison of t_o(s) Obtained at 200 RPM.

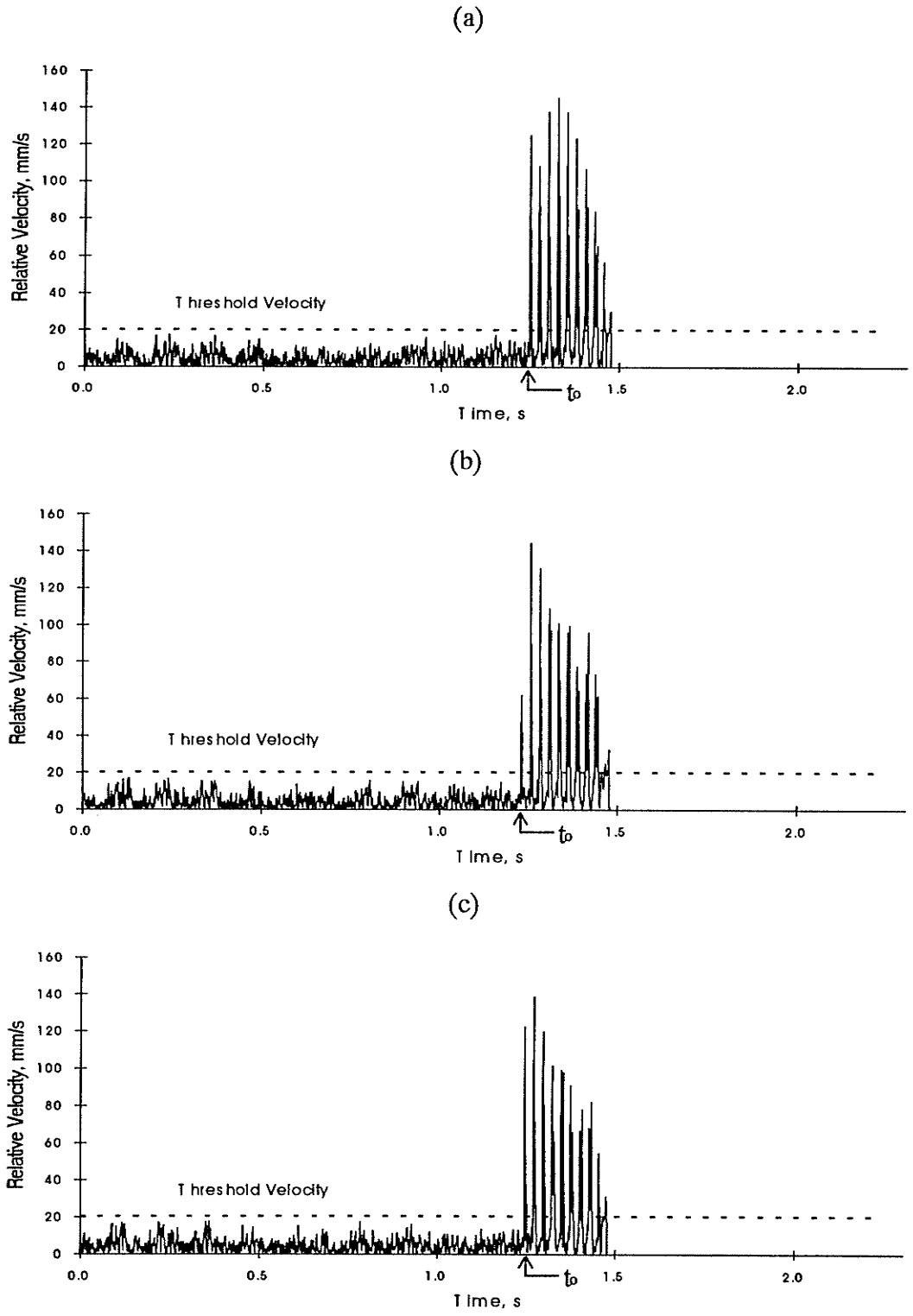

Figure 4.9. A Comparison of t_o(s) Obtained for the Same Cylinder Rotating at 2289 RPM.

4.3.1.2 Command of the Scanning Speed

The scanning speed of 0.3 mm/s used in the experimental configuration is restricted by the stepper motor's speed as well as its maximum of 150 oz-in torque. The 0.3 mm/s scanning speed corresponds to the 2 s duration for the arm to sweep up and down as well as the computational time of 1 s for each 1 mm increment in the distance of the prototype device along the Z-axis, $S_{z\text{-axis}}$. Suppose, next, that the prototype device is to be employed in a real time feedback turning system. This means that the device must travel with the tool post along the Z-axis at the rough turning feedrate. The maximum rough turning feedrate can vary widely. It depends upon the workpiece's material, the cutting tool's material, and the lathe's power. Conservatively speaking, it could be as fast as 3 mm/s. Although, there is no doubt that the scanning speed can be increased substantially by using a stepper motor or servo motor with sufficient torque, the adverse cutting conditions such as cutting fluid and "flying" chips always remain the biggest issue in applying a laser-based device in a metal cutting environment. Therefore, measurements taking between cuts is the best way to use a laser-based measurement device until a new technique is discovered that can avoid these adverse cutting conditions.

4.3.2 Effect of Laser's Spot Size and Travel Increment

The RMS difference, in mm, between the reference and measured profiles along some critical region, such as corner or step, relates to the laser's spot size, ϕ_{laser}, and the increment in the distance of the prototype device along the Z-axis, $S_{z\text{-axis}}$. The RMS difference is employed to measure how much the measured profile lies from the reference profile under the influence of ϕ_{laser} and $S_{z\text{-axis}}$. It is defined, in reference [20], by

$$\mathrm{RMS} = \left[\frac{1}{N} \sum_{k=1}^{N} |\Delta_k|^2 \right]^{1/2}. \tag{4.3}$$

Here N is the number of stations obtained by dividing the critical region in equal horizontal steps. The Δ_k, in mm, is the difference in distance between the reference and measured profiles at each station k. A symmetrical object, for instance a cylinder, having a step change, Δr, in its cross-sectional radius has been selected as an example. Three measured profiles from the same reference profile were obtained by using 1.0, 0.5 and 0.25 mm for $S_{z\text{-axis}}$. The reference and measured profiles are described in Figure 4.10(a) by solid and dotted line, respectively, at different values of $S_{z\text{-axis}}$. To evaluate the RMS difference between the reference and measured profiles along the critical region corresponding to the stepped change in cross-sectional data, both profiles were divided artificially into ten equally separated, horizontal layers, i.e. a total of eleven stations so that N=11. Although better approximation can be obtained by using a higher number of layers, ten is sufficient for illustrative purpose. The profile measured by using $S_{z\text{-axis}}$=1.0 mm is enlarged and displayed in Figure 4.10(b) together with the corresponding differences, Δ_k, for demonstration. The Δ_k were calculated straightforwardly and substituted into equation (4.3) to give a RMS difference of $0.3\phi_{laser}$ mm. RMS difference of $0.3\phi_{laser}$ and $0.4\phi_{laser}$ mm were also calculated when $S_{z\text{-axis}}$ was changed from 1.0 mm to 0.5 and 0.25 mm, respectively. Thus, a reduction in $S_{z\text{-axis}}$ does not necessarily improve the measurement accuracy along the critical region. Therefore, the RMS difference along the critical region can be reduced only certainly by employing a lower ϕ_{laser} (i.e. a smaller laser spot).

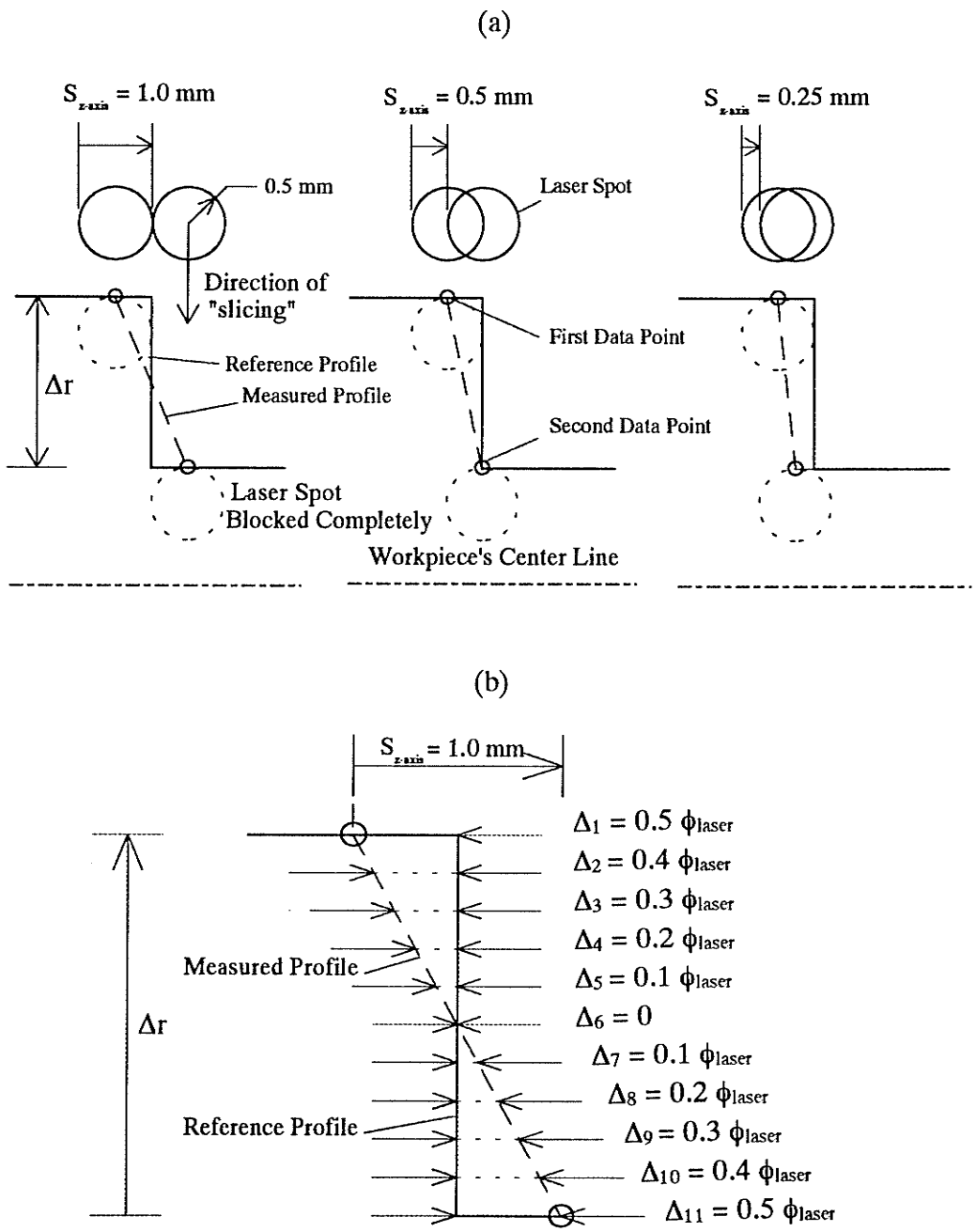

Figure 4.10. (a) Change in Measured Profiles at Different Increments along the Z-axis, and (b) Example of Calculation of the RMS Difference Between the Reference and Measured Profiles at $S_{z\text{-axis}}$=1.0 mm.

4.4 Results of Profile Mapping

The results of scanning three different workpieces are given in Figures 4.11, 4.12 and 4.13. The first two workpieces were manufactured with ± 0.03 mm accuracy by using

the EMCO CNC machine. Their reference dimension was obtained by using a caliper with an accuracy of 0.01 mm. The last workpiece was a small tree branch that had both an eccentricity and protrusions. The reference dimension, which was measured by using a caliper, had an accuracy of about 0.5 mm because the unevenly "soft" wood contracted slightly and variably when pressured by the contracting.

Figure 4.11(a) compares the measured and reference upper profiles of a symmetrical object having three vertically sided grooves. The corresponding % errors in the cross-sectional diameters along the object's length are given in Figure 4.11(b). This figure shows that the maximum error was less than 1.4 %. It also clearly confirms that a laser having a 1 mm diameter circular spot distorts critical regions such as a step diametrical change. Figure 4.12 gives an analogous comparison but for a symmetrical workpiece having more gently curved contours. However, the maximum error in the shaft's diameter increased from about 1.4 % to a still acceptable 2.3 % for rough turning.

Figure 4.13 presents an example of mapping both the inside and outside spinning profiles of an asymmetrical workpiece, the small tree branch. By comparing the mapped and reference profiles, a maximum 9.5 % and 2.5 % error was found in the outside and inside profiles, respectively. The inside profile's minimum radius of 8.2 mm indicates that the maximum allowable radius, R in Figure 2.1, of 8.2 mm can be manufactured from the workpiece, even though a radius of 13.5 ± 0.5 mm was measured when the workpiece was stationary. The eccentricity of 5 mm along the workpiece can be approximated by measuring the distance between the physical and rotational center shown in Figure 4.13(a). Furthermore, the outside profile's maximum radius of 28.9 mm determines the tool offset, C_{offset} in Figure 2.1, to avoid a collision at the sudden change in profile.

(a)

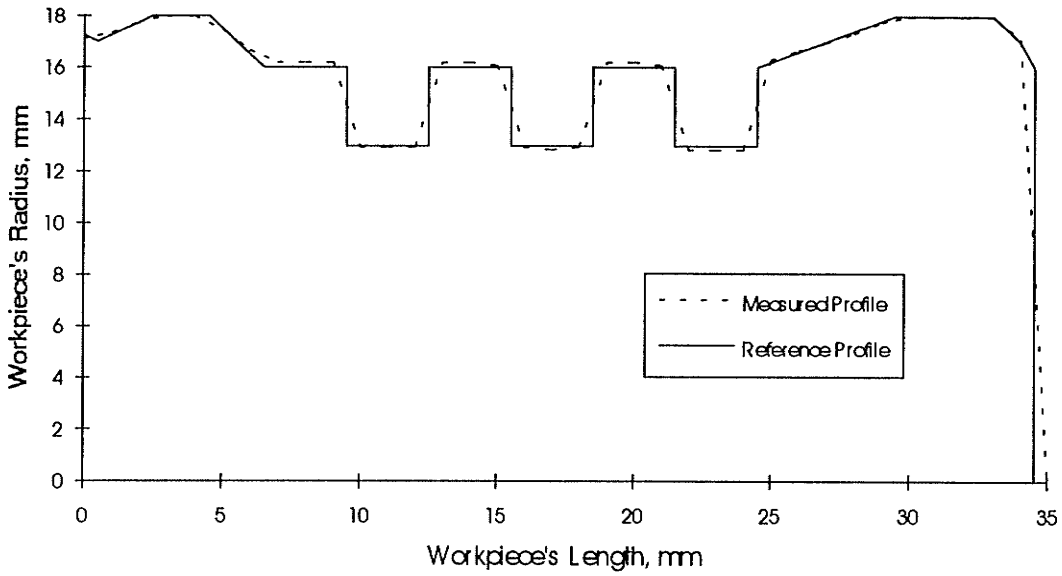

(b)

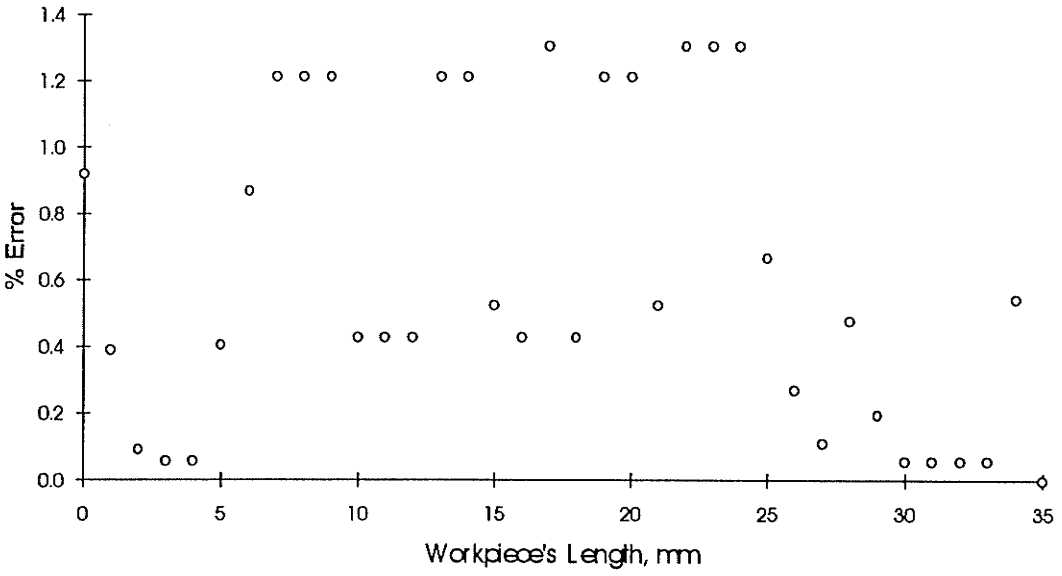

Figure 4.11. Showing (a) Comparison of Measured and Reference Step Profiles, and (b) % Error in Diameter along the Workpiece's Length.

(a)

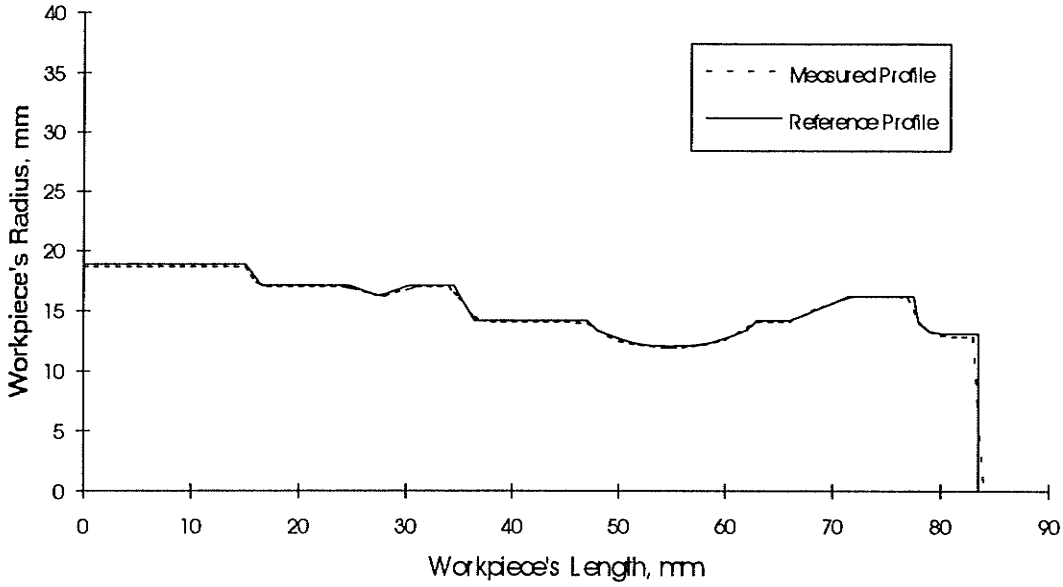

(b)

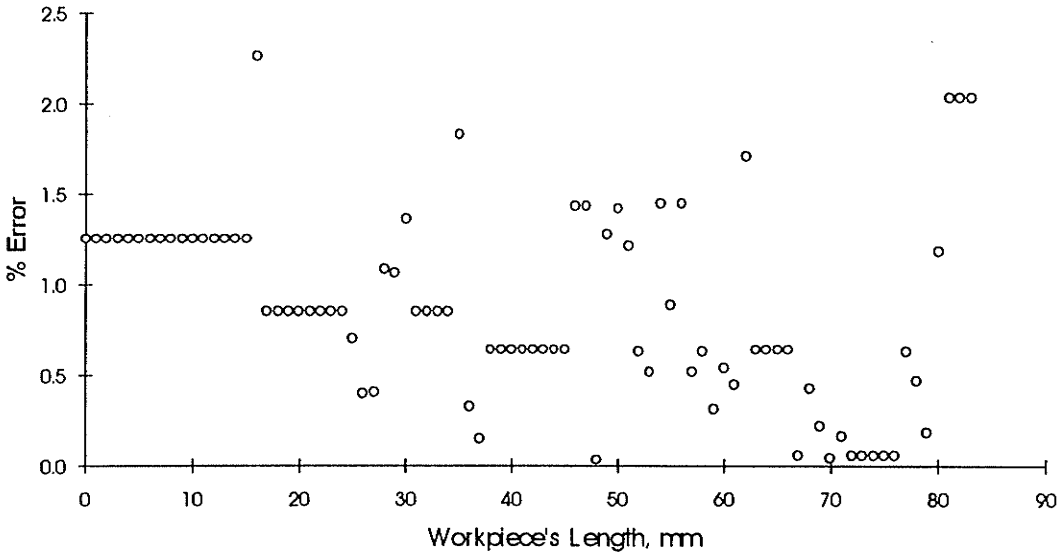

Figure 4.12. Showing (a) Comparison of Measured and Reference Profiles, and (b) % Error in Diameter along the Workpiece's Length.

(a)

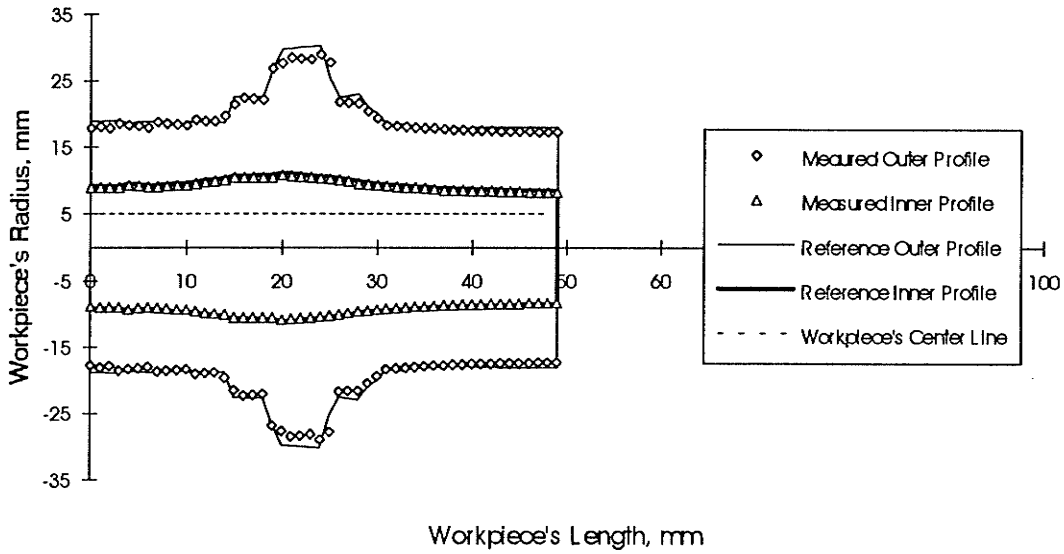

(b)

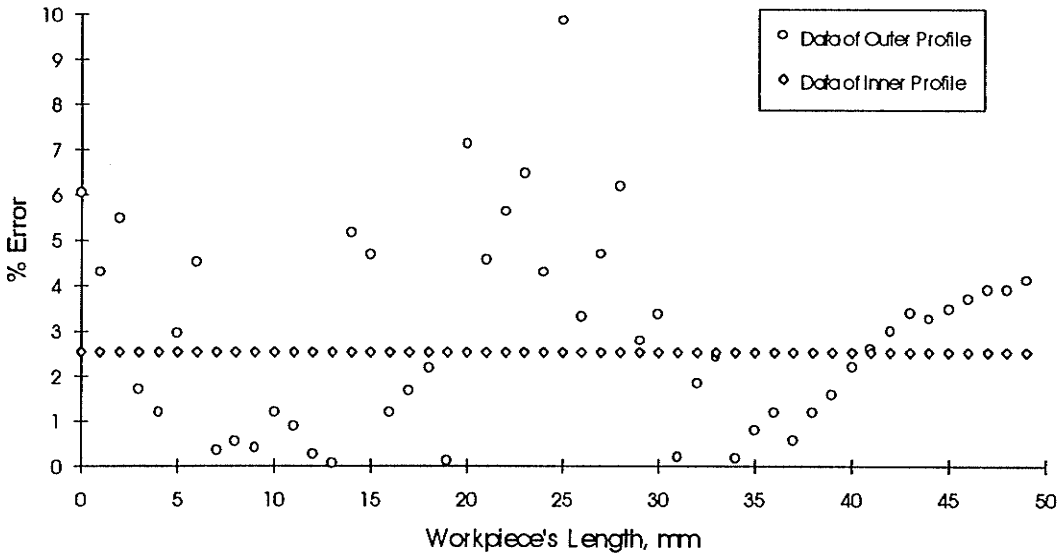

Figure 4.13. Showing (a) Inner and Outer Profiles of a Spinning, Asymmetrical Workpiece, and (b) % Error in Diameter along the Workpiece's Length.

4.5 Results of Automation and New Cutting Strategy

A system in which human effort is eliminated from a process is regarded as fully automated. In today's manufacturing environment, the initial dimensions of a raw material to be turned in a lathe are usually determined by human effort. After the prototype device is attached to a computer control lathe, the effort required from an operator to confirm a dimension is no longer needed. Once the scanning is completed, two files containing the relocation sequence of the cutting tool for conventional and modified cutting are generated. Besides, the total cutting time required for each strategy is displayed on the screen of a microcomputer so that an operator can select which cutting strategy is to be used. Furthermore, the minimum cross-sectional diameter is also displayed for a preliminary quality inspection.

Two cutting tests were conducted on the workpiece illustrated in Figures 4.11(a) and 4.12(a), and a time saving of up to 36 % was obtained compared with conventional cutting which was determined through a simulation. The optimal solutions were generated heuristically for the relocation sequence of the cutting tool for the given workpieces. The solutions are shown in Figures 4.14 and 4.15. The workpieces were both manufactured with an accuracy of ±0.5 mm to cylinders close but less than their minimum scanned diameters. The final diameters were 25.0 mm and 23.0 mm. Cutting parameters were calculated by using the procedures described in Section 3.2 of Chapter 2 after properly selecting the workpiece's material from the computerized data base. A feedrate of 0.22 mm/rev and a cutting speed of 58 m/min were used invariably. The duration spent on cutting each designated travel segment was recorded and the results are tabulated in Table 4.2 for completeness.

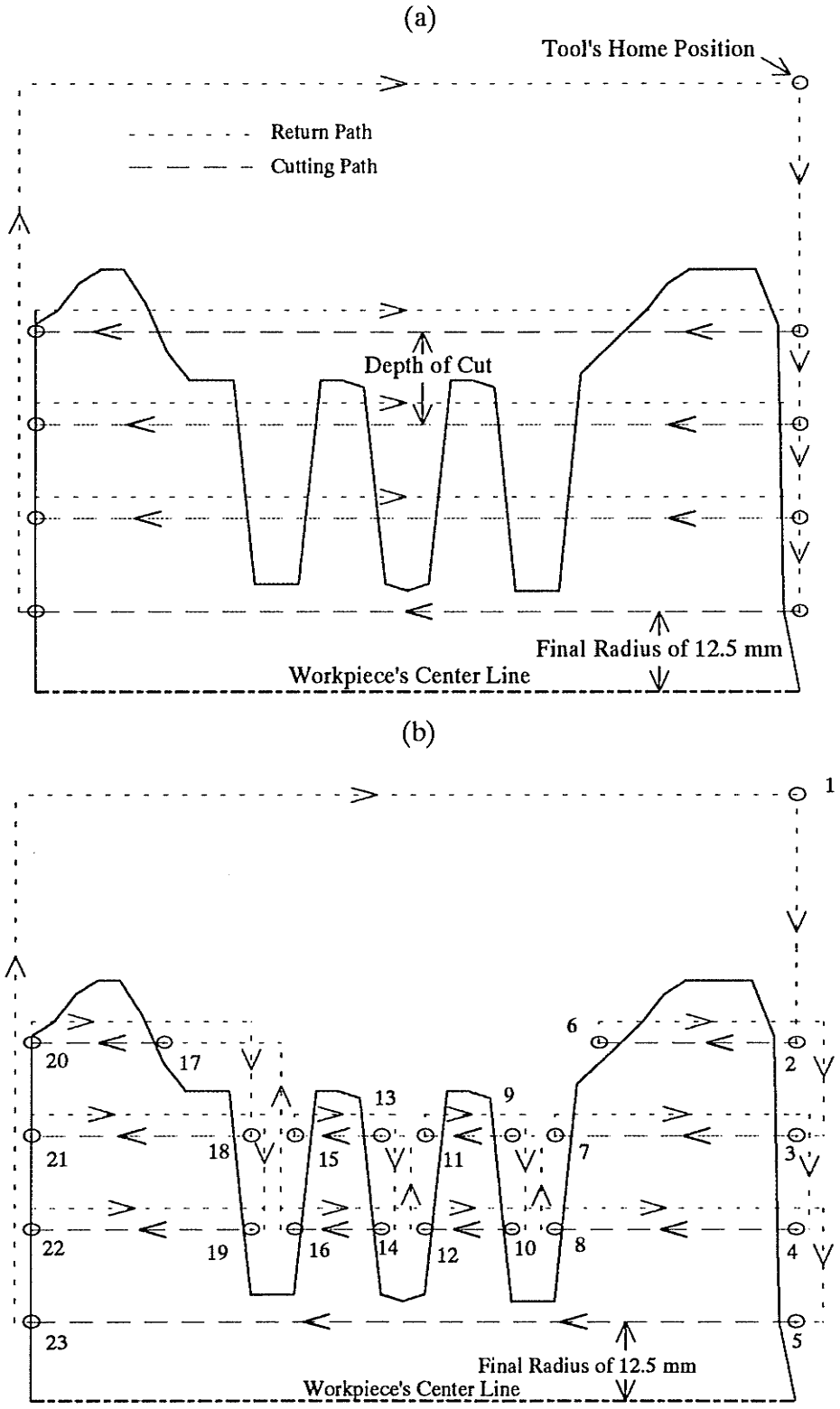

Figure 4.14. Comparison of Tool Paths Between (a) Conventional and (b) Optimal Solution for the Profile of Figure 4.11(a).

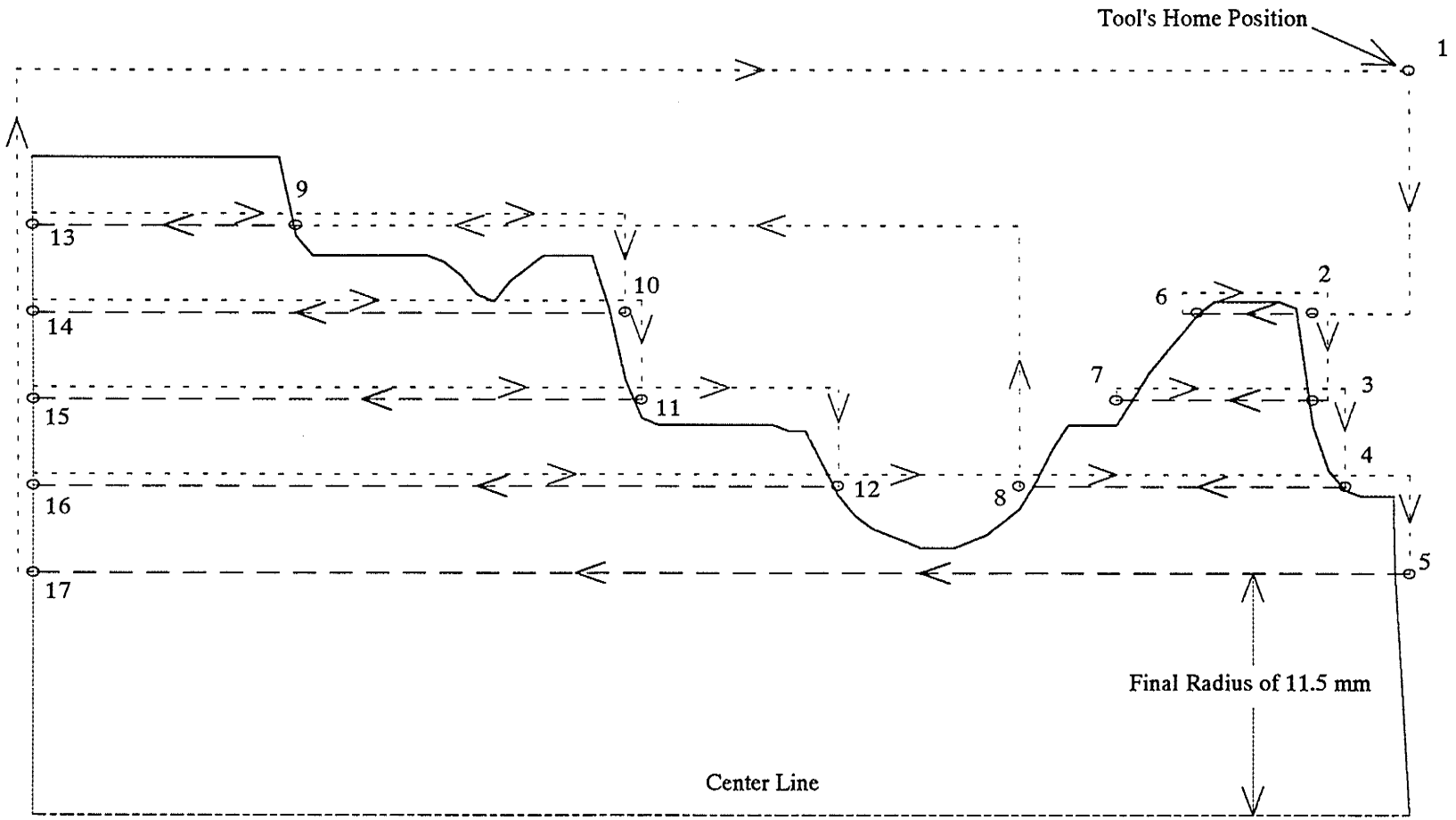

Figure 4.15. Optimal Tool Path for Profile of Figure 4.12(a).

$T_{1,2}$=0.44	$T_{2,6}$=4.52	$T_{6,3}$=1.16	$T_{3,7}$=5.53	$T_{7,4}$=1.38	$T_{4,8}$=5.53
$T_{8,9}$=0.39	$T_{9,11}$=2.01	$T_{11,10}$=0.61	$T_{10,12}$=2.01	$T_{12,13}$=0.39	$T_{13,15}$=2.01
$T_{15,14}$=0.61	$T_{14,16}$=2.01	$T_{16,17}$=0.99	$T_{17,20}$=3.01	$T_{20,18}$=1.27	$T_{18,21}$=5.02
$T_{21,19}$=1.27	$T_{19,22}$=5.02	$T_{22,5}$=4.03	$T_{5,23}$=17.58	$T_{23,1}$=4.81	

(a)

$T_{1,2}$=0.63	$T_{2,6}$=3.62	$T_{6,3}$=0.97	$T_{3,7}$=6.20	$T_{7,4}$=1.76	$T_{4,8}$=2.82
$T_{8,9}$=5.52	$T_{9,13}$=8.27	$T_{13,10}$=4.27	$T_{10,14}$=18.61	$T_{14,11}$=4.38	$T_{11,15}$=19.13
$T_{15,12}$=5.74	$T_{12,16}$=25.33	$T_{16,5}$=9.73	$T_{5,17}$=43.43	$T_{17,1}$=10.69	

(b)

Profile	Time Spent in Cutting, s		% Time Saved
	Conventional Approach	New Strategy	
Figure 4.14(b)	87.7	71.6	**18.3**
Figure 4.15	267.2	171.1	**36.0**

(c)

Table 4.2. Time (in s) Spent on Travelling Each of the Segments shown in (a) Figure 4.14(b), (b) Figure 4.15, and (c) the Time Saved by the New Cutting Strategy.

4.6 Results of Vibration Detection

Although the prototype device should be sensitive only to light that is interrupted by the workpiece, vibration caused by unbalance during the cutting was also detected by the experimental setup shown in Figure 4.1. A preliminary experiment to assess the device's capability to detect vibration was undertaken by using the lathe. A vibration was induced by an eccentric mass (about 10 g) which was attached to a shaft and spun at 658 RPM (11.0 Hz) and then at 1159 RPM (19.3 Hz). The speeds were verified by a digital stroboscope. To avoid aliasing in the data sampling, the sampling frequency must be at least twice the highest frequency of interest [24]. Therefore, the sampling frequency of

the AD converter was set to 1 kHz, and the output signal was recorded over 1.2 s. The resulting time varying signals from the sensor are presented in Figure 4.16. The plots show the anticipated periodic patterns. The lowest frequencies are approximately 11 and 19 Hz due to the unbalanced centrifugal force. The higher frequency corresponds to a disturbance produce by electrical noise during the measurement. In conclusion, the prototype device can be developed further as a vibration measurement device.

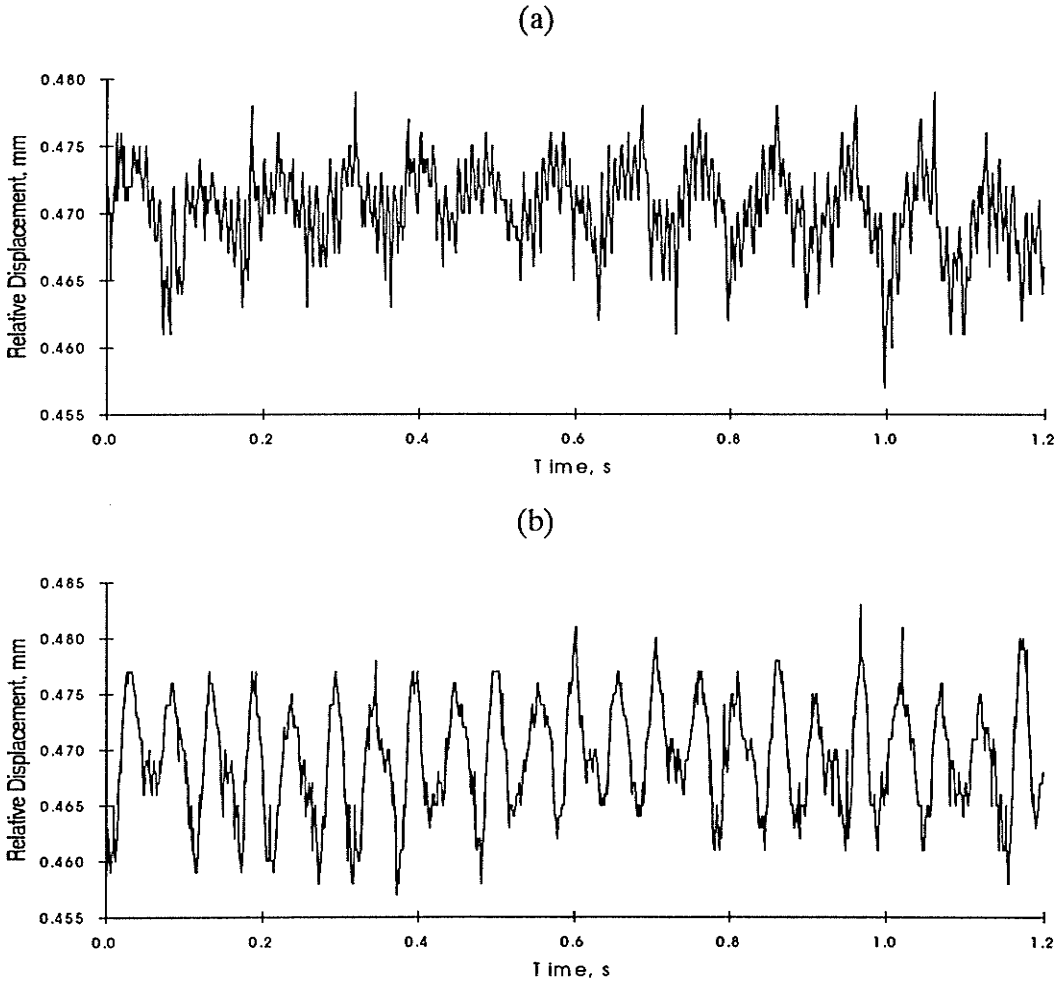

Figure 4.16. Showing the Displacement at a Spindle Speed of (a) 658 RPM (11.0 Hz), and (b) 1159 RPM (19.3 Hz).

4.7 Results of Chatter Suppression

The previously described vibration tests led to the development of closed-loop control to suppress chatter. This development was demonstrated by the following experiment in which the same setup used in the vibration tests was employed. However, instead of capturing the extraneous vibration caused by the eccentric mass, the extraneous vibration induced while cutting was captured.

4.7.1 Relating Extraneous Vibration to Different Depth of Cuts

Four slender low carbon steel bars, each having a 25.4 mm (1") diameter and 381 mm (15") length, were used to increase the flexibility of the workpiece so that the chatter could occur more easily. Hence, the assumption of a rigid workpiece is no longer valid. The bars were cut separately at the same feedrate of 1.24 mm/s and a spindle speed of 658 RPM. However, different constant cutting depths of 3.0, 4.0, 4.5 and 5.0 mm were employed. Four hundred samples of the vibration signal from the prototype device were recorded over a 1.6 s cutting period and the results are displayed in Figure 4.17. The difference between the minimum and maximum relative displacement is designated as Rd_{max} in this figure. A relationship is shown in Figure 4.18 between Rd_{max} and a given constant depth of cut. This plot suggests that feedback control is needed when the depth of cut is higher than 4 mm because excessive vibration will result, and the vibration magnitude of 0.08 mm should indicate a normal cutting condition. Therefore, the depth of cut can be modified by monitoring the change in Rd_{max}. Excessive noise was also noticed but only when the 5 mm depth of cut was used. Then, chatter marks were also visually observed later. These observation confirm that a large depth of cut can produce chatter.

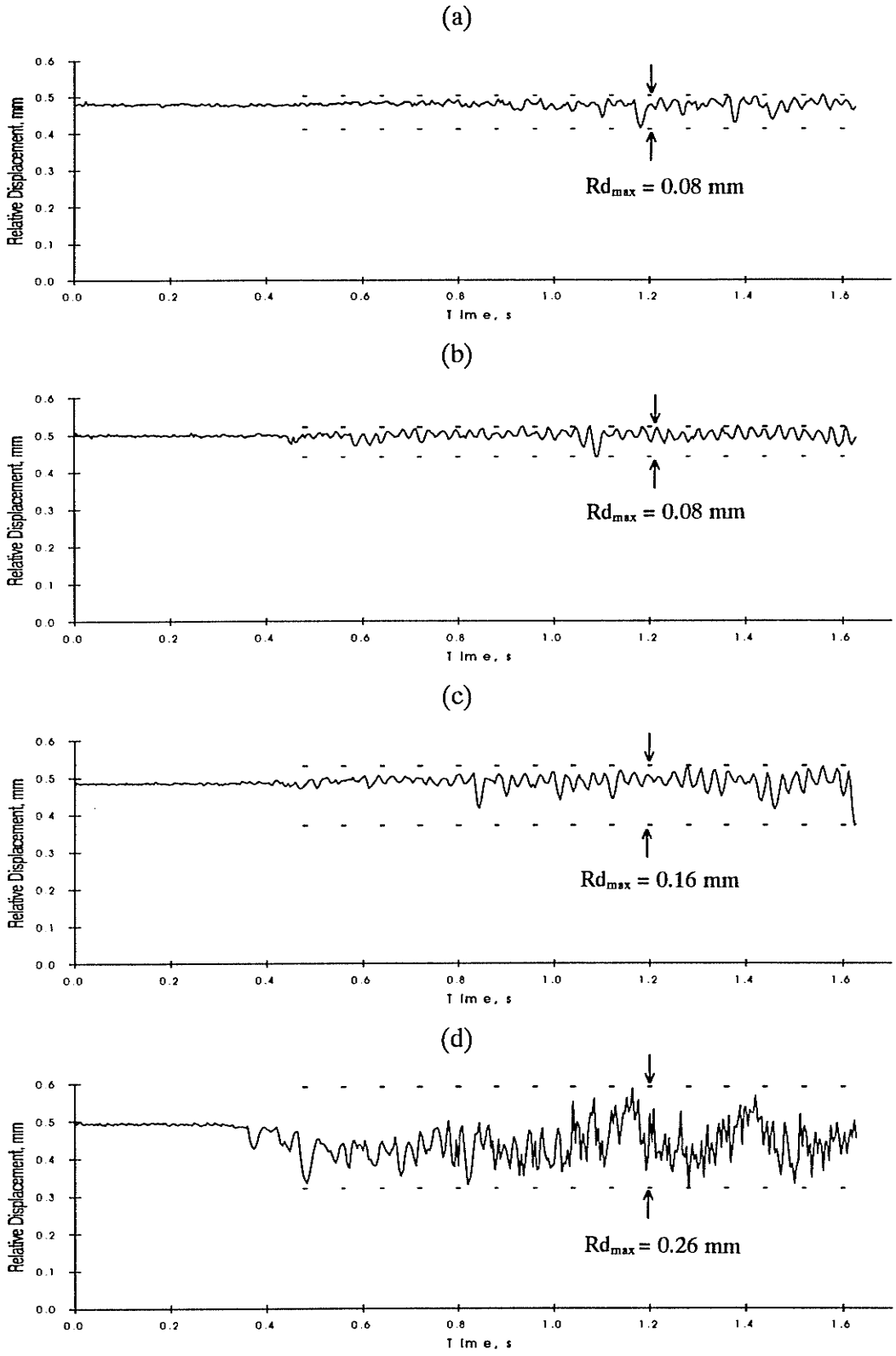

Figure 4.17. Cutting Signal when Depths of Cut were a Constant (a) 3.0 mm, (b) 4.0 mm, (c) 4.5 mm, and (d) 5.0 mm.

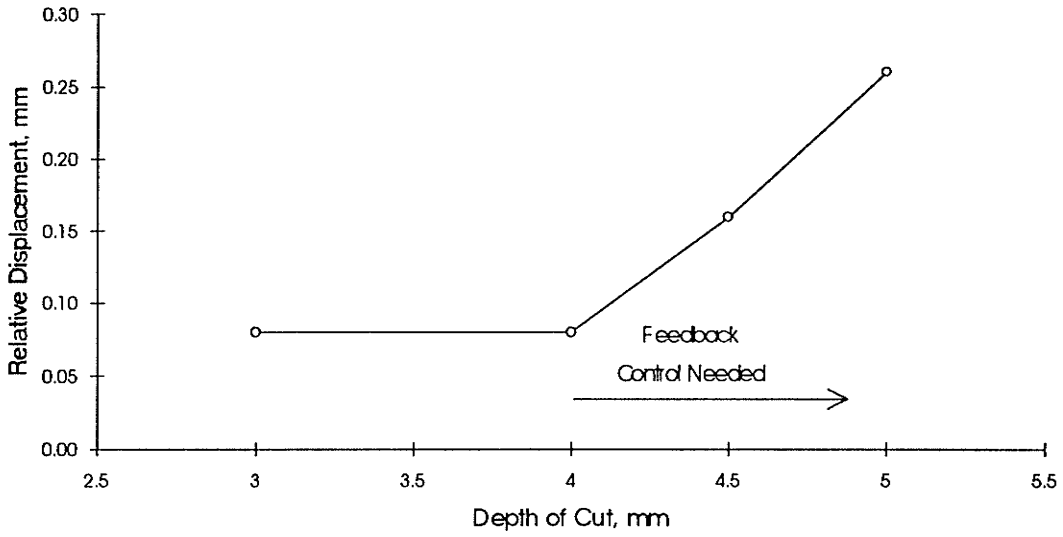

Figure 4.18. Relationship Between Depth of Cut and Rd_{max}.

4.7.2 Closed-loop Control To Suppress Extraneous Vibration

The results of cutting with different depths of cut suggested that Rd_{max} could be used to indicate excessive vibration. Therefore, software was written to monitor Rd_{max} by comparing its value during cutting with a preset threshold value. In this experiment, the same setup was used except that a servo motor was activated to control the depth of cut whenever Rd_{max} was higher than a threshold value. The threshold value of 0.08 mm was selected because this value was obtained when using the 3 mm depth of cut without any noticeable problems. Moreover, a 3 mm depth of cut was suggested in reference [8] for maximum conservative cutting. If Rd_{max} was higher than the 0.08 mm threshold value, then the depth of cut was decreased, otherwise the depth of cut remained constant. In this cutting test, a longer cutting period of 7.3 s was used. The initial 5 mm depth of cut was expected to be reduced gradually until the extraneous vibration was alleviated.

In this automatic chatter suppression process, the software recorded the output signal and controlled the depth of cut if Rd_{max} was higher than the threshold value. The signal captured during the cutting period is plotted in Figure 4.19.

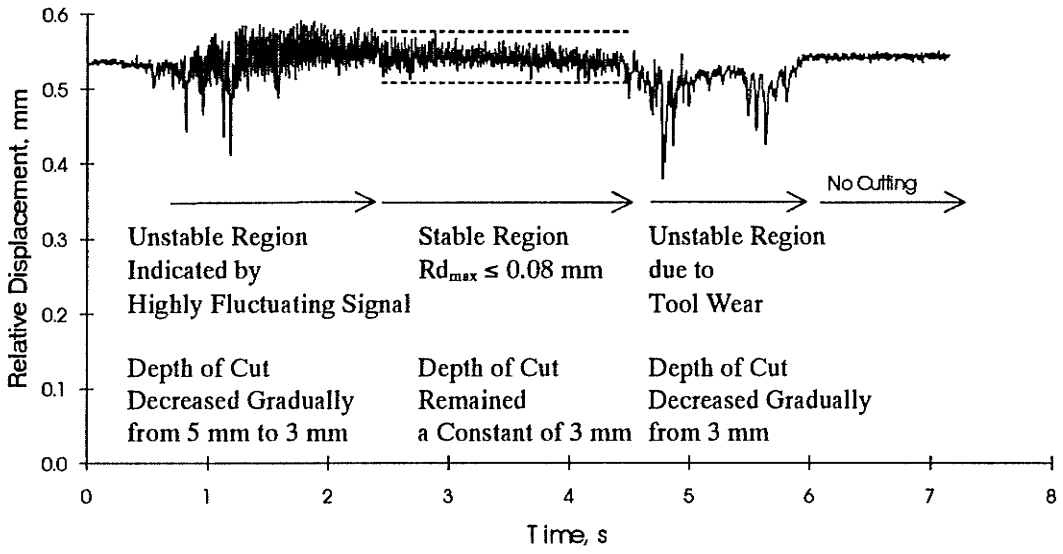

Figure 4.19. Output when Depth of Cut was Modified.

The output signal in this figure can be divided into the four regions which are indicated by arrows. In the first region, excessive vibration was initiated at 0.9 s. Consequently, a high Rd_{max} was recorded and the depth of cut began to reduce. This action finally stopped, until the measured Rd_{max} fell below the threshold value of 0.08 mm, at 2.5 s. The depth of cut had been readjusted already from 5 mm to 3 mm. In the second or stable region, the depth of cut remained at a constant 3 mm for about 2.1 s, at which time excessive vibration reoccurred. Hence, the depth of cut was reduced again within the third region until the high vibration was suppressed. At about 6.1 s, the tool was separated from the workpiece. Therefore, the final region contained only a slightly fluctuating signal until the end of the 7.3 s sampling period.

The reoccurrence of the excessive vibration (despite the depth of cut being adjusted below 3 mm) was investigated further by examining the cutting tool. In fact, a built up edge of about 3 mm was found along the tool's cutting edge. Thus, the vibration's reoccurrence might have been caused by the high friction between this built up edge and

the workpiece. Therefore, this preliminary experiment suggested that the prototype device can be used to monitor an unpredictable cutting situation.

4.8 Detection of Tool Breakage

Finally, a cutting test demonstrated that the prototype device was capable of detecting tool breakage. A low carbon steel having a 25.4 mm (1") diameter and 381 mm (15") length was selected for the experiment to detect of tool breakage. A high speed steel tool was used to cut the workpiece which was spun at 658 RPM (corresponding to a cutting speed of 52.5 m/min). A feedrate of 1.24 mm/s (or 0.113 mm/rev) and a cutting depth of 3 mm were selected based on the criteria stated in Chapter 3. The combination of these cutting parameters would require a 1.3 kW motor power (calculated by using equations (3.1) and (3.2)) which was nearly the maximum capacity of the experimental lathe. Therefore, an undersized cutting tool was more likely to break because of the ensuing large cutting force.

The cutting process was set to last for 3.2 s during which eight hundred data samples were recorded. If the cutting tool did not break during the cutting process, the process was repeated and a new set of data was recorded. Tool breakage occurred during the fourth cut. The signal generated when the tool broke was captured and it is plotted in Figure 4.20. A signal resulting from a normal cutting condition can be observed from this plot before 1.8 s. The cutting tool's breakage was indicated by a sudden change in Rd_{max}. If the signal's fluctuation level reduced after 0.5 s, then there was a high chance that a tool breakage had occurred. Hence, the prototype device could be applied to the detection of tool breakage in rough turning.

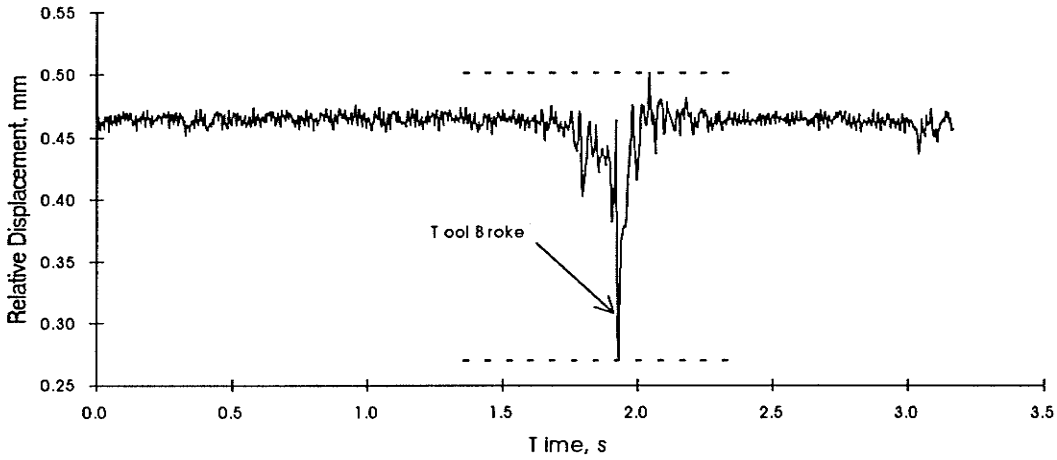

Figure 4.20. Signal Indicating Tool Breakage.

CHAPTER 5
CONCLUSIONS AND RECOMMENDATIONS

Cutting results showed that the new cutting system can handle any shaped workpiece, and can also improve the material removal rate, MRR, in rough turning by as much as 36 % compared with conventional cutting. This reduction was achieved by knowing the workpiece's spinning profile in advance and by employing a new cutting strategy. The new strategy simply minimized the tool's total travel distance and increased the feedrate, based on the mapped workpiece's profile. The use of a heuristic for determining the tool's minimal total travel distance was validated by solving the same problem with the use of an integer programming technique. The cutting system was also equipped with an automatic retrieval function of cutting parameters.

The spinning profile of any symmetrical or asymmetrical workpiece can be mapped automatically by the prototype device, regardless of the workpiece's surface roughness, color or surface orientation. Measurements indicated that the percent error in the workpiece's radius varied between 0.1 to 2.3 % for symmetrical workpieces. The prototype also had the capability to map spinning profiles of a highly irregular, asymmetrical workpiece with an accuracy better than 9.5 %.

The automation of single part production in turning is not available in today's manufacturing environment. Hence, manual machining is preferred for the duplication of a part. If the part has a unique profile which is difficult to obtain manually, then remanufacturing the part may be difficult. The prototype device can be used to obtain such a profile within a reasonable period. However, the prototype must provide a measurement accuracy better than ±0.03 mm, which is the standard accuracy in finish turning. There is a possible refinement to increase the measurement accuracy of the present prototype device that is to use a more sensitive photocell. Moreover, eight kinds

of common single-point lathe tools are required for a standard lathe operation [25]. They are illustrated in Figure 5.1. Therefore, a automatic tool retrieval system is needed.

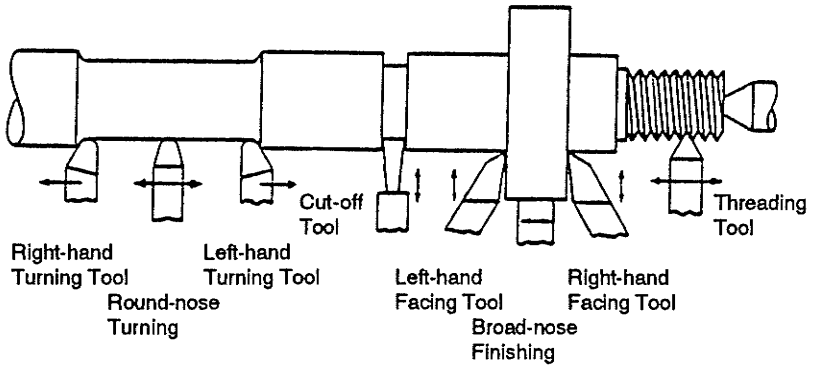

Figure 5.1. Shapes and Uses of Common, Single-point Lathe Tools.

Furthermore, several excellent preliminary results indicated that the prototype device can be used to monitor extraneous vibration and tool breakage. Promising experimental results were also obtained in the development of closed-loop control to suppress chatter by using this device during rough turning. Consequently, the prototype device can improve safety in rough turning.

Although 267.2 s – 171.1 s = 96.1 s (see Table 4.2(c)) was reduced in rough turning a 83 mm long workpiece (see Figure 4.15), an extra $\frac{83}{0.3} = 277$ s was required to complete the scanning at the present maximum speed of 0.3 mm/s. Consequently, the manufacturing cycle time was increased by 277 s – 96 s = 181 s. However, the scanning speed can be improved substantially by modifying the present prototype device. For example, the stepper motor can be replaced by a faster one. Besides, a line light source and linear CCD sensor can be used to replace the complex prototype mechanism and convert a point source to a line source. If the scanning speed can be increased only ten times (from 0.3 to 3.0 mm/s), then a new scanning time will become $\frac{83}{3.0} = 28$ s. A time

reduction of $96\,s - 28\,s = 68\,s$ in the overall manufacturing cycle will result after the scanning speed is improved. Hence, the new turning system will accomplish a $\frac{68}{267.2} \times 100\,\% = 25\,\%$ overall time reduction.

An optimized machining control system should continuously adjust basic machining data for an optimal operation, regardless of process changes during the operation. Furthermore, a continuous update of the workpiece's dimensions will guarantee that the resulting product will meet specifications and that time wastage due to tool wear or breakage will be reduced. Besides, cutting parameters can be updated continuously based on the new dimensions after each cut. However, a real time dimensional feedback system cannot be formed unless problems from adverse cutting conditions due to "flying" chips and cutting fluid are solved. Consequently, a scan between each cut is suggested presently.

In conclusion, it is possible to build an intelligent material turning system which has the flexibility and efficiency required for today's manufacturing.

REFERENCES

[1] D. Yan, "Measurement and Prediction of Surface Roughness in Finish Turning", Ph.D. Thesis, University of Manitoba, Department of Mechanical and Industrial Engineering, 1993.

[2] J.E. Kaye, D. Yan, N. Popplewell, S. Balakrishnan, and D.J. Thomsom, "Electronic System for Surface Roughness Measurements in Turning", International Journal of Electronics, Vol. 69(6), 1993, pp.835-848.

[3] D. Yan, J.E. Kaye, S. Balakrishnan, and N. Popplewell, "Surface Roughness Measurement in Finishing Turning", International Journal of Advanced Manufacturing Technology, accepted. Nov. 1995.

[4] D. Yan, J.E. Kaye, N. Popplewell, and S. Balakrishnan, "On-line Prediction of Surface Roughness in Finish Turning", Engineering Design and Automation Journal, accepted Oct. 1995.

[5] D. Yan, M. Cheng, N. Popplewell, and S. Balakrishnan, "Real-time Roughness Measurements of a Finish-turned Surface", International Journal of Production Research, accepted Oct. 1995.

[6] R. Toutant, S. Balakrishnan, S. Onyshko, and N. Popplewell, "Feedrate Compensation for Constant Cutting Force Turning", IEEE Control Systems, Vol. 13(6), 1990, pp.44-47.

[7] Stephen M. Copley, "Laser Shaping of Materials", American Society for Metals, Conference Proceedings, pp.82-92.

[8] "Machining Data Handbook, 3rd Edition", Institute of Advanced Manufacturing Sciences, Inc., 1980.

[9] S. Motavalli and B. Bidanada, "A Part Image Reconstruction System for Reverse Engineering of Design Modifications", Journal of Manufacturing Systems, Vol. 10(5), 1991, pp.383-395.

[10] R.J. Hunsicker, J. Patten, A. Ledford, C. Ferman, and M. Allen, "Automatic Vision Inspection and Measurement System for External Screw Threads", Journal of Manufacturing Systems, Vol. 13(5), 1994, pp.370-384.

[11] A.K. Asundi, C.S. Chan, and M.R. Sajan, "360-deg Prfilometry: New Techniques for Display and Acquisition", Optical Engineering, Vol. 33(8), August 1994, pp.2760-2769.

[12] D.W. Manthey, K.N. Knapp, and D. Lee, "Calibration of a Laser Range-Finding Coordinate-Measuring Machine", Optical Engineering, Vol. 33(10), October 1994, pp.3372-3380.

[13] G.K. Jaisingh and F.P. Chiang, "Contouring by Laser Speckle", Applied Optics, Vol. 20(19), October 1981, pp.3385-3387.

[14] K. Harding, E. Sieczka, E. Kaltenbacher, and A. Boehnlein, "Design of an On-machine Gage for Diameter Measurements", SPIE, Vol. 1821, 1992, pp.439-446.

[15] E. Zussman, H. Schuler, and G. Seliger, "Analysis of the Geometrical Features Detectability Constraints for Laser-Scanner Sensor Planning", International Journal of Advanced Manufacturing Technology, 1994, pp.56-64.

[16] M. Jouaneh, R.L. Lemaster, and D.A. Dornfeld, "Measuring Workpiece Dimensions Using a Non-Contact Laser Detector System", International Journal of Advanced Manufacturing Technology, 1987, pp.59-74.

[17] M. Hohda, "Method of and Apparatus for Measuring Radius", Applied Optics, Vol. 25(15), August 1986, pp.2452-2452.

[18] F.M. Smolka and T.P. Caudell, "Surface Profile Measurement and Angular Deflection Monitoring using Scanning Laser Beam: a Noncontact Method", Applied Optics, Vol. 17(20), October 1978, pp.3284-3289.

[19] P. Saint-Marc, J.L. Jezouin, and G. Medioni, "A Versatile PC-Based Range Finding System", IEEE Transactions on Robotics and Automation, Vol. 7(2), April 1991, pp.250-256.

[20] J.H. Mathews, "Numerical Methods for Computer Science, Engineering, and Mathematics", Prentic-Hall, Inc., 1987.

[21] W.L. Winston, "Operations Research: Application and Algorithms", PWS-KENT Publishing Company, Boston, 1990, pp.412-416.

[22] C. Gadsby, S. Balakrishnan and N. Popplewell, "A Microcomputer-based Controller for Milling Machines", International Journal of Advanced Manufacturing Technology, Vol. 4(2), May 1989, pp.168-181.

[23] K. Timothy, "Development of a Flexible, Mircocomputer Based, Three-Axis Machine Tool Controller", M.Sc. Thesis, Department of Mechanical and Industrial Engineering, University of Manitoba, 1988.

[24] W.H. Press, S.A. Teukolsky, W.T. Vetterling, and B.P. Flannery, "Numerical Recipes in C, The Art of Scientific Computing, Second Edition", Cambridge University Press, 1992, pp.500-501.

[25] "Materials and Processes in Manufacturing", Collier-MacMillan Limited, London, 1969, pp.524-525.

Appendix A.

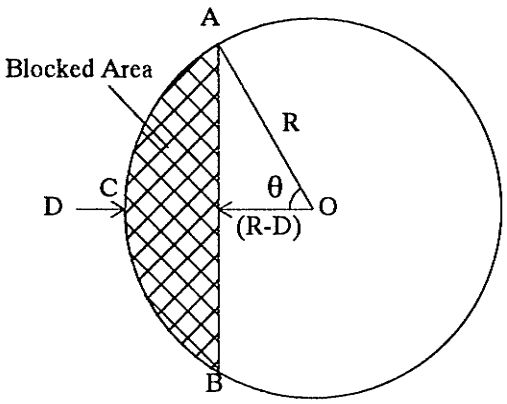

$$\cos\theta = \frac{R - D}{R},$$

$$\therefore \theta = \cos^{-1}\left(\frac{R - D}{R}\right).$$

$$\text{Sector OAB} = \pi R^2 \times \frac{2\theta}{360}.$$

Figure A.1. Side View of a Laser Beam Blocked by an Object.

If D<R, then Area ABC = Sector OAB - Triangle OAB

$$= \frac{\theta\pi R^2}{180} - (R - D)R\sin\theta.$$

$\therefore$ Percent Reduction of Spot, dA

$$= \frac{\frac{\theta\pi R^2}{180} - (R - D)R\sin\theta}{\pi R^2} \times 100\%. \qquad (2.1a)$$

If D>R, then Area ABC = Sector OAB + Triangle OAB

$$= \frac{\theta\pi R^2}{180} + (R - D)R\sin\theta.$$

$\therefore$ Percent Reduction of Spot, dA

$$= \frac{\frac{\theta\pi R^2}{180} + (R - D)R\sin\theta}{\pi R^2} \times 100\%. \qquad (2.1b)$$

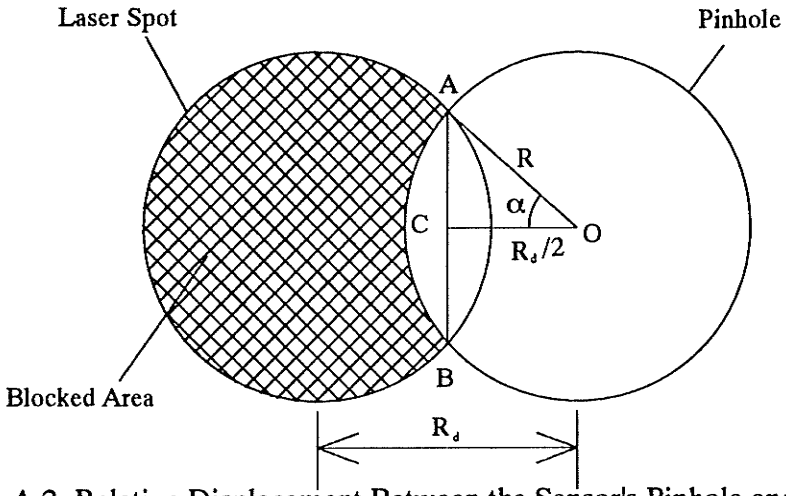

Figure A.2. Relative Displacement Between the Sensor's Pinhole and the Laser Spot.

$$\cos\alpha = \frac{\frac{R_d}{2}}{R},$$

$$\therefore\ R_d = 2R\cos\alpha. \qquad (2.2)$$

Area ABC = Sector OAB - Triangle OAB

$$= \frac{\alpha\pi R^2}{180} - \frac{R_d}{2} R\sin\alpha.$$

Now, $R_d = 2R\cos\alpha.$

$$\therefore \text{ Area ABC} = \frac{\alpha\pi R^2}{180} - R^2\cos\alpha\sin\alpha.$$

$\therefore$ Area of Sensor Received Light = 2×Area ABC

$$= \frac{\alpha\pi R^2}{90} - 2R^2\cos\alpha\sin\alpha.$$

Area of Sensor Received Light = (1- Percent Reduction of Spot Area)×πR^2,

$$\Rightarrow \frac{\alpha\pi R^2}{90} - 2R^2\cos\alpha\sin\alpha = \pi R^2\left(1 - \frac{dA}{100}\right),$$

$$\therefore \frac{\alpha\pi}{90} - 2\cos\alpha\sin\alpha = \pi\left(1 - \frac{dA}{100}\right). \qquad (2.3)$$